

Electrical characterization of nanoparticle and protein networks

Holovchenko, Anastasia

DOI

[10.4233/uuid:4b1f83ad-df5c-4f7f-9dde-d3ea2a6b79ec](https://doi.org/10.4233/uuid:4b1f83ad-df5c-4f7f-9dde-d3ea2a6b79ec)

Publication date

2017

Document Version

Final published version

Citation (APA)

Holovchenko, A. (2017). *Electrical characterization of nanoparticle and protein networks*. [Dissertation (TU Delft), Delft University of Technology]. <https://doi.org/10.4233/uuid:4b1f83ad-df5c-4f7f-9dde-d3ea2a6b79ec>

Important note

To cite this publication, please use the final published version (if applicable). Please check the document version above.

Copyright

Other than for strictly personal use, it is not permitted to download, forward or distribute the text or part of it, without the consent of the author(s) and/or copyright holder(s), unless the work is under an open content license such as Creative Commons.

Takedown policy

Please contact us and provide details if you believe this document breaches copyrights. We will remove access to the work immediately and investigate your claim.

**ELECTRICAL CHARACTERIZATION OF
NANOPARTICLE AND PROTEIN NETWORKS**

ELECTRICAL CHARACTERIZATION OF NANOPARTICLE AND PROTEIN NETWORKS

Proefschrift

ter verkrijging van de graad van doctor
aan de Technische Universiteit Delft,
op gezag van de Rector Magnificus prof. ir. K.C.A.M. Luyben,
voorzitter van het College voor Promoties,
in het openbaar te verdedigen op dinsdag 4 juli 2017 om 12:30 uur

door

Anastasia HOLOVCHENKO

Master of Science in Physical and Biomedical Electronics, Sumy State University, Sumy,
Ukraine
geboren te Sumy, Ukraine.

This dissertation has been approved by the promotor

Prof. dr. ir. H. S. J. van der Zant

Composition of the doctoral committee:

Rector Magnificus, Prof. dr. ir. H. S. J. van der Zant	voorzitter Technische Universiteit Delft
---	---

Independent members:

Prof. dr. H. W. Zandbergen	Technische Universiteit Delft
Prof. dr. M. Dogterom	Technische Universiteit Delft
Prof. dr. P. J. Peters	Maastricht University
Prof. dr. ir. L. M. K. Vandersypen	Technische Universiteit Delft
Prof. dr. P. G. Steeneken	Technische Universiteit Delft



Keywords: charge transport, two-terminal measurements, protein conductance, biosensors, protein networks, nanoelectrodes

Printed by: Gildeprint - Enschede

Front & Back: A.Holovchenko

Copyright © 2017 by A. Holovchenko
Casimir PhD series, Delft-Leiden 2017-23

ISBN 978-90-8593-307-6

An electronic version of this dissertation is available at
<http://repository.tudelft.nl/>.

*It is only with the heart that one can see rightly;
what is essential is invisible to the eye.*

Antoine de Saint-Exupery

1

INTRODUCTION

In this chapter, a classification of nano-objects is introduced. The starting point is to give a definition of nano-objects and classify them by means of size and material they are made of. After that, we discuss ways of studying physical and chemical properties of these objects. Finally, we describe known applications of nano-objects in electronics and biosensing and suggest new ways of their operation.

1.1. CLASSIFICATION OF NANO-OBJECTS

People throughout time have been trying to understand and explain the environment they live in. Driven by this curiosity, and most importantly by finding answers to the questions “Why?” and “How?”, scientists have made a chain of brilliant discoveries in physics, chemistry and biology. However, there is still more to discover. Feynman’s lecture “There’s plenty of room at the bottom” given in 1959 drew attention of the scientific world to the physics at the nanoscale (10^{-9}m). In subsequent years, scientific tools were getting more and more advanced allowing to reveal the hidden properties of very small objects such as DNA, proteins or molecules, which was not possible before. In this thesis, these small objects will be referred to as “nano-objects”. Importantly each object has its own unique size, shape and properties, most of which are yet to be discovered.

One may ask: “How do scientists study nano-objects if they are so small?” At the beginning, they did that simply by visual inspection, i.e., by observing it. Of course, because the objects are so small, it cannot be done by the bare eye and special tools have to be used. If one wants to know the size or the shape of a nano-object, transmission-electron microscopy (TEM) is the best tool to go for. In a TEM an beam reaches the specimen which contains the small object. Based on electron-specimen interaction an image is formed, from which the size and shape of the object can be extracted. In Chapter 2 different technologies used for studying nano-objects are described in more details.

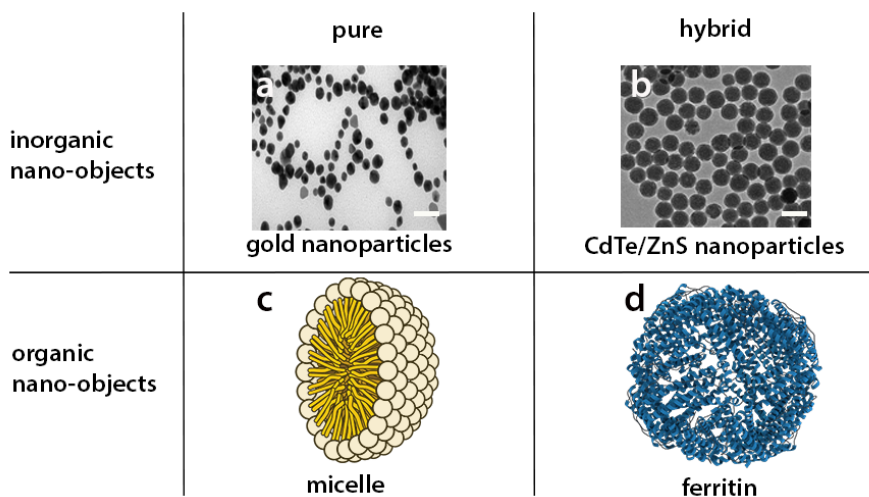


Figure 1.1: Material-based classification of nano-objects: (a) Transmission electron microscopy (TEM) image of gold nanoparticles representing inorganic nano-objects. Scale bar is 50 nm. Image adapted from [1]. (b) TEM image of CdTe/ZnS nanoparticles with an average size of 30 nm. Image adapted from [2]. Scale bar is 50 nm. Organic nano-objects represented by (c) a micelle,[3] which is a supramolecular assembly with hydrophilic regions. (d) Metalloprotein ferritin contains both an organic shell and a ferrihydrite mineral core, which contains about 4500 iron (Fe^{3+}) atoms. Image adapted from.[4]

The material composition of nano-objects can be either inorganic or organic, with metallic (e.g. gold) nanoparticles and semiconducting (e.g. GaAs) quantum dots being examples of the former. Organic nano-objects (e.g. polypeptide chains of a protein)

are generally speaking less conductive than metallic ones, but they are biologically compatible and mostly come from nature or can be chemically synthesized. In addition, to the above-mentioned examples, there is another subset of nano-objects that has both organic and metallic components, which can be called hybrid nano-objects. This class is extremely interesting because it combines both biocompatibility of the organic components and the high conductivity of the metallic part. Figure 1.1 shows nano-object classification based on the material composition. Several examples of such objects will be described in this thesis in Chapter 4, Chapter 5 and Chapter 6.

1.2. CHARACTERIZATION AND APPLICATION OF NANO-OBJECTS

Once the size and shape are defined, one could perform a more detailed characterization of the physical and chemical properties. One of the ways of addressing a small object is to conduct “electrical measurements” on them. Like with electron microscopy, in this method a signal is sent into the nano-object (e.g. an electron flow at a pre-set bias voltage) and the readout signal is received back when the electrons have passed through it and the current is measured. The difference between the “input” and “output” signal might indicate a unique feature of the object that can be then translated to, for instance, a “real” biological meaning, although this is often a challenging task. Characterizing nano-objects in any way would give us more insight on how they function, which is a rather fundamental question.

On the other hand, it turns out that small objects with unique features can be applicable, for example in electronics. Transistors, the main building blocks of electronics, are smaller and “smarter” with every following generation. But each technology has limitations, and for transistors built with silicon technology, this is their size and the heat consumption. The idea of using small nano-objects, such as molecules or nanoparticles, came after the limitations of Si-based technology became obvious.[5] The proposed diode-like current-voltage (I-V) characteristic calculated in 1974 by Aviram and Ratner[6] opened the door to the molecular nanoworld, and led to the formation of a whole new field that is now called Molecular Electronics. Scientists became driven by the idea that electronic components can be scaled down even more by using single molecules or nanoparticles.

The success of Molecular Electronics in making single-molecule transistors,[7] logic gates[8, 9] and memory devices[10] brought up another idea to use biological species as components for electronic circuits. In fact, the first experiment in this field goes back to 18th century with Luigi Galvani and his experiment on frog legs. That was the first proof that animal tissues can transfer electricity. But this so called “animal electricity” phenomenon faced criticism and got forgotten till 1943,[11] when the experiments in the field of biological voltaic electricity were renewed. The first steps in the field of Bioelectronics[12, 13] were made while studying electrical transmission through cells[14] and neurons[15] integrated into a solid-state chip platform.

This unique technology[16, 17] not only allowed to integrate the protein onto the chip and potentially use it as an electronic component, but also to study its chemical and physical properties; it thereby gave insight in a number of important biological processes, such as respiration and photosynthesis[18].

1.3. THESIS OUTLINE

The outline of this thesis is as follows:

In Chapter 2 we give an overview of the main technologies for nanogap formation, which are then widely used for contacting nano-objects. Detailed description of graphene electroburning and e-beam lithography techniques are also given in this chapter.

In Chapter 3 we show that graphene electrodes formed by electroburning technique can be used for contacting single diamo-terphenyl molecule. The pre-patterning of the electrodes by He-ion beam milling allows to localize the nanogap and to reduce the number of the molecules attached to the electrodes after deposition. The electrical measurements showed molecular signature in current and gate-voltage-dependent characteristics at low temperature.

Chapter 4 presents a near-room temperature memory effect in spin-crossover(SCO) nanoparticles. Single-layer graphene electrodes formed using electron-beam lithography were used for contacting the nanoparticles. Reproducible hysteresis in conductance (in temperature range of about 40 K) related to the spin-transition was observed. The low-spin state had a noticeably higher conductance than the high-spin state.

In Chapter 5 a set of electrical measurements of hemoglobin protein networks is shown. The protein network is connected to platinum electrodes with a 100 nm separation. The environmental-dependent current change was observed during the electrical characterization. In particular, the current drops to below the noise level in vacuum and shows a decrease up to an order of magnitude when exposed to nitrogen gas instead of air.

Chapter 6 we show the electrical characterization of Alzheimer's ferritin networks from human brain and compare it to the physiological one at ambient conditions. The networks with the two types of proteins coupled to platinum nanoelectrodes, showed different levels of conductance. Particularly, the conductance of the samples with Alzheimer's ferritin is consistently lower than those composed of physiological protein. When a nitrogen atmosphere was introduced the conductance of both protein networks went below the detection limit of the setup.

REFERENCES

- [1] Retrieved February 2, 2017, from www.nature.com/articles/srep05593/figures/2.
- [2] Retrieved February 2, 2017, from <http://www.nature.com/nprot/journal/v6/n8/abs/nprot.2011.357.html>.
- [3] Retrieved February 2, 2017, from <https://commons.wikimedia.org/wiki/File:Michelle.svg>.
- [4] Retrieved February 2, 2017, from <http://2013.igem.org/Team:Calgary/Project/OurSensor/Reporter/PrussianBlueFerritin>.
- [5] Schulz, M., *The end of the road for silicon?*, Nature **399**, 729–730 (1999).
- [6] Aviram, A. and Ratner, M. A., *Molecular rectifiers*, Chem. Phys. Lett. **29**, 277–283 (1974).
- [7] Carter, F. L., *The molecular device computer: Point of departure for large scale cellular automata*, Phys. Nonlinear Phenom. **10**, 175–194 (1984).
- [8] de Silva, A. P. and Uchiyama, S., *Molecular logic and computing*, Nat. Nanotechnol. **2**, 399–410 (2007).
- [9] Kompa, K. L. and Levine, R. D., *A molecular logic gate*, Proc. Natl. Acad. Sci. U. S. A. **98**, 410–414 (2001).
- [10] Robinson, B. H. and Seeman, N. C., *The design of a biochip: a self-assembling molecular-scale memory device*, Protein Eng. **1**, 295–300 (1987).
- [11] Focaccia, M. and Simili, R., *in Brain, Mind and Medicine: Essays in Eighteenth-Century Neuroscience*, 145–158 Springer US, (2007).
- [12] Szent-Györgyi, A., *Bioelectronics*, Science **161**, 988–990 (1968).
- [13] Rivnay, J., Owens, R. M. and Malliaras, G. G., *The Rise of Organic Bioelectronics*, Chem. Mater. **26**, 679–685 (2014).
- [14] Hess, L. H. et al., *Graphene transistor arrays for recording action potentials from electrogenic cells*, Adv. Mater. Deerfield Beach Fla **23**, 5045–5049, 4968 (2011).
- [15] Patolsky, F. et al., *Detection, Stimulation, and Inhibition of Neuronal Signals with High-Density Nanowire Transistor Arrays*, Science **313**, 1100–1104 (2006).
- [16] Freedman, K. J., Haq, S. R., Edel, J. B., Jemth, P. and Kim, M. J., *Single molecule unfolding and stretching of protein domains inside a solid-state nanopore by electric field*, Sci. Rep. **3**, 1638 (2013).
- [17] Otten, M. et al., *From genes to protein mechanics on a chip*, Nat. Methods **11**, 1127–1130 (2014).
- [18] Lambers, H., Iii, F. S. C. and Pons, T. L., *in Plant Physiological Ecology*, Springer New York **11–99** (2008).

2

NANOELECTRODES FOR CONTACTING NANO-OBJECTS

In this chapter we introduce different approaches for the fabrication of nano-electrodes and give some details on the several nano-objects that are further described in this thesis. The chapter begins with an overview of existing technologies for the fabrication of such electrodes and the areas of their application. We zoom in and explain the advantages of two techniques in particular (electroburning of 2D materials and e-beam lithography) which allow to contact nanoparticle- and protein networks, used for the experiments described in the subsequent chapters of this thesis. In the second part, we introduce the three different types of nano-objects used in this thesis work, describe their properties and discuss points of interest for further research.

2.1. DEVICE FABRICATION

2

Contacting an individual nano-object, such as a protein or a nanoparticle in a network has been a technological challenge lasting for decades. The development of scanning tunnelling microscopy (STM), [1–4] atomic force microscopy (AFM), [5] break-junctions [6, 7] and advances in nanofabrication [8] allowed to get insight into the world of these objects. Figure 2.1 summarizes the techniques which are used for contacting nano-objects of different size; the smallest object can be found on the left-hand side. The size and structure of these objects can be determined directly (by observing via microscopy tools) or indirectly (e.g. by measuring the electrical response of a signal that was sent in via scanning probes or on-chip by micron-sized electrodes). Some technologies from Figure 2.1 are more suitable for particular configurations of nano-objects [9]. For instance, with STM one can study individual particles, but the technique is not as effective for particle arrays, as high-atomic resolution and a large scan range are generally not compatible with each other. On the other hand, Electron-beam Lithography (e-beam) is a reliable tool for fabricating devices on chip and contacting arrays of nano-objects; this technology is limited to features of about 10 - 20 nm and larger.

In Figure 2.1 the red rectangulars indicate three main technologies that were used as tools for making the nano-electrodes described in this thesis. One of them, called electroburning [10, 11], opens up unique possibilities for studying both nanometre-thick organic films and individual nanoparticles [12] or proteins. In essence, it allows to form a gap with nanometre-spacing between the electrode pair [13–17] by ramping the voltage across a graphene bridge while the current is monitored. The high voltage in combination with Joule heating “breaks” the structure of the material at the nano-level, and this break can be observed as a drop in the conductance at the macro-scale. In Figure 2.2 the fabrication scheme of the multi-layer graphene electrodes fabricated using nanofabrication and electroburning is displayed. The gap, however, can appear anywhere in the device (depending on the shape of the device, defects in the lattice of the material, etc.) and the size of the gap is not controlled. For studying electrical properties of nano-object networks the area of the gap can be in order of a few micrometres, but when scaling down to the single-protein level, the gap has to be smaller and preferably localized at a particular spot of the sample. Pre-patterning (or shaping) of a device before electroburning allows to localize the gap and to narrow down the possible contact area between the molecules and the electrodes [18]. The pre-patterning can be done using resist coating and electron-beam lithography or by direct milling with an ion beam.

For studying nano-objects whose size is larger than 20 nm, electron-beam lithography can be used for nanogap formation. The resolution limit of this technology currently is 10 - 20 nm [19, 20], which does not allow to contact individual molecules or proteins because of their size, but is suitable for contacting organic nanometre-thick films [21] or nanoparticles connected in series [22]. An example of this process is shown in Figure 2.3. The fabrication process usually starts with a Si wafer covered with SiO_2 . The wafer is spin-coated with a positive or negative electron-sensitive film – a resist. A digital pattern of the nanodevice is then transferred onto the resist surface using an electron-beam. In case of a positive resist, the area that was exposed under the e-beam becomes soluble to a resist developer and can be removed from the surface of the wafer. Now, a layer of metallic film can be created using metal evaporation. As the metallic film cov-

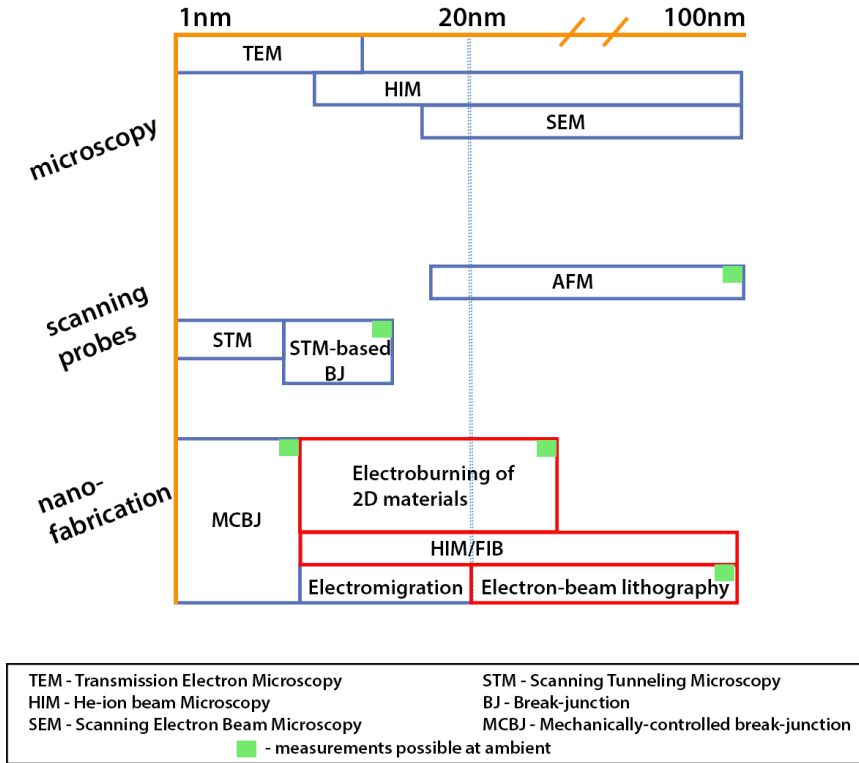


Figure 2.1: The main technologies (Y-axis) used for characterization of solid-state proteins and nanoparticles of different size (X-axis). The technologies are arranged in groups as follows: 1) Microscopy tools, used for observing and determining the size and shape of the nanoobject, 2) Scanning probes, used for direct contacting individual nanoobjects by establishing an electrical connection between the object and the metallic tip, and 3) Nanofabrication, also used for direct contacting of small and big nanoobjects by placing them onto a fabricated chip with contacts. The green square in the top right corner of a box around a particular technology indicates that the measurement/observation can be done at ambient condition (room temperature and atmospheric pressure). A red rectangular around a technique highlights a technology that will be further described in this thesis.

ers the whole wafer a lift-off process is applied in order to reveal the pattern previously written via the e-beam. The lift-off also dissolves the resist buried under the thin metal film, thereby defining the device. The main limiting factors of this technique are: i) e-beam spot size ii) proximity effects, related to the exposure dose distribution iii) the use of resist, which can leave residuals on the surface after fabrication. More information on e-beam lithography approach can be found in Chapter 4, Chapter 5 and Chapter 6 of this thesis. In Chapter 4 we show how a single-layer graphene device with a nanogap

made by e-beam lithography can be used for contacting spin-crossover nanoparticles. In Chapter 5 and Chapter 6 platinum electrodes fabricated by e-beam lithography are used for electrical characterization of protein networks.

2

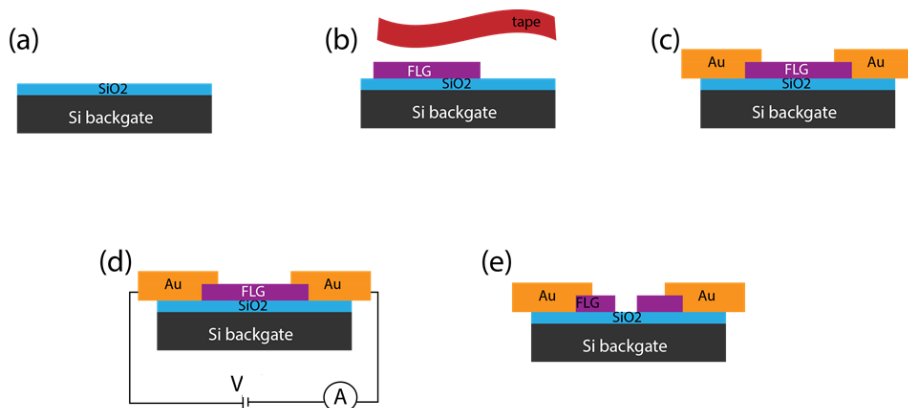


Figure 2.2: Fabrication scheme of a few-layer graphene (FLG) nano-electrode device with the gap made by electroburning.

(a) The fabrication starts with heavily-doped Si chips (19x19 mm²) with a 285-nm thick layer of SiO₂ film on top.

(b) Graphene is exfoliated onto the substrate using the “scotch-tape” method. Flakes of desirable thickness (approx. 7 nm) are then selected under the optical microscope by means of colour.

(c) Positive resist (PMMA) is spin-coated on top of the chip at 4500 rpm and baked for 7 minutes at 180°C. Areas for Au contacts are then exposed with an electron beam, developed in a methyl isobutyl ketone (MIBK) : isopropanol (IPA) 1:3 solution for 90 seconds and in IPA for 30 seconds. Subsequent metal evaporation (Temescal FC-2000) of 5 nm Ti and 80 nm Au is done at a base chamber pressure of 10^{-6} mbar. This step finishes by lift-off in hot acetone at 52°C for 30 minutes.

(d) Feedback-controlled electromigration performed on the fabricated chip at ambient conditions. While the voltage (up to 10 V) is ramped up across the flake, the induced high-current densities increase the temperature of the flake, and carbon atoms start to react with oxygen. Feedback-controlled software monitors the conductance, and repeats the cycle of the voltage ramp till the resistance of the flake is larger than 10 GOhm.

(e) The nanogap in a FLG device is formed.

He-ion beam milling (HIM) does not require spinning a resist on a substrate and can be used as an alternative to e-beam lithography. The concept of this technique is similar to Focused Ion beam (FIB) milling, but instead of heavy Ga atoms in the FIB, lighter He atoms are used in HIM. In HIM, ionized He atoms are accelerated before reaching the surface of the sample.

A high energy and the acceleration of the He ions allow to remove atoms from the lattice of the sample. As a result, a few-nanometre sized gap can be formed. The main disadvantage of this technology is that the obtained high-atomic precision is not as effective for long nanogaps, as the size of the ion beam is small and as a consequence it would take too much time to write it without having to compensate for the drift of the

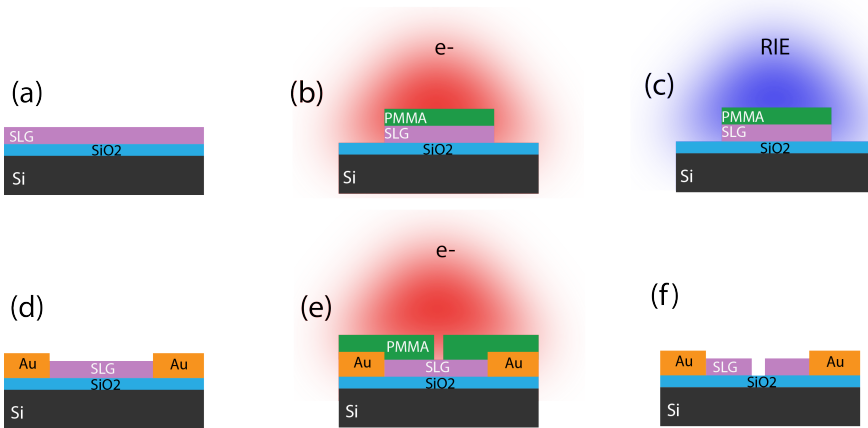


Figure 2.3: Fabrication scheme of a single-layer graphene (FLG) device with a gap made by e-beam lithography. (a) The fabrication begins with Si/ SiO₂ (285-nm) chip (10 x 10 mm₂) with commercially grown single-layer graphene on top.

(b) In order to make contact pads the chip is covered with PMMA resist at 4500 rpm and baked for 7 min at 180°C. Areas for Au contacts are then exposed with an electron beam (dose 900 $\mu\text{C}/\text{cm}^2$), and developed in a MIBK:IPA 1:3 solution for 90 seconds and subsequently in IPA for 30 seconds.

(c) Reactive ion etching (Leybold Heraeus) is performed with a gas flow of 25 sccm of O₂, a pressure of 50 μBar and a power of 20 W for 30 seconds. The oxygen plasma yields an anisotropic etch of single-layer graphene and allows to perform metal deposition of contact pads on SiO₂.

(d) Next, 5 nm of Ti and 40 nm of Au are deposited using metal evaporation (conditions similar to Figure 2 (c)). In this step the metallic contact pads are fabricated.

(e) Nanogap definition. The chip is covered with PMMA, exposed to an electron beam (dose 1200 $\mu\text{C}/\text{cm}^2$) and developed in MIBK:IPA (similar to step (b)).

(f) In order to open the nanogap RIE is used (same parameters as in step (c)), followed by lift off in hot acetone for 30 minutes.

beam. Figure 2.4 shows the device before and after pre-patterning with the He-ion beam, where the two trenches define a constriction of 500nm wide. Also, pre-patterning allows to fabricate and electroburn several devices connected to the same pair of electrodes (see Figure 5). In Chapter 3 we describe in the detail the advantages of pre-patterning with the He-ion beam and localization of the gap.

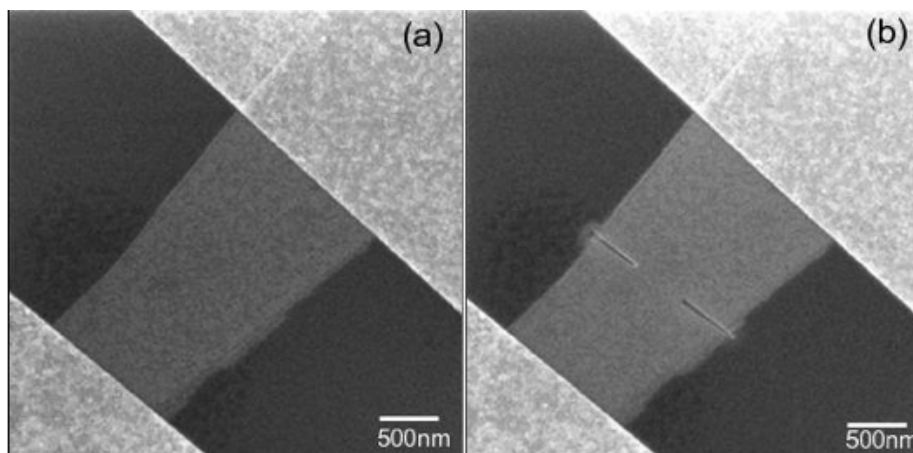


Figure 2.4: Scanning-electron microscopy (SEM) image of a FLG device before pre-patterning (a) and after pre-patterning (b) with He-ion beam milling. Two trenches made with the ion beam allow the gap to be localized at the narrowest part of the flake.

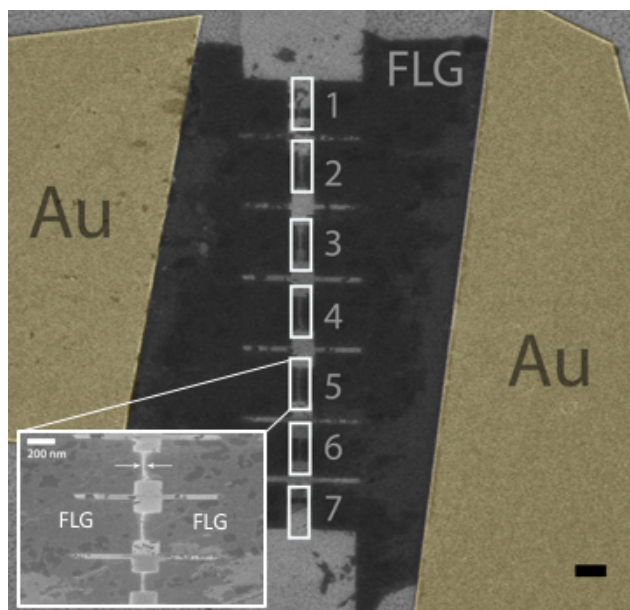


Figure 2.5: Scanning electron microscopy (SEM) image (false colour) of a FLG device that consists of seven pre-patterned bridges that were electroburned. Scale bar is 200 nm. Inset: Zoom-in SEM image of nanogap 5,6 and 7 from the main figure. The white arrows indicate where nanogap 5 is located on the bridge. Scale bar is 200 nm.

2.2. DEVICE CHARACTERIZATION

Once contact to a nano-object has been established a set of questions concerning their (electrical) characterization arises:

- (i) What is the reproducibility of contacting the same nano-object?
- (ii) How to define the orientation of the nano-object once it has been attached to the electrodes?
- (iii) What is the electronic coupling between the nano-object and the electrodes?
- (iv) Which charge transport mechanism is dominant in this system?

One way of answering these questions would be to perform electrical measurements, for instance current-voltage characteristics (two-terminal measurements), or electrical measurements as a function of applied gate voltage (three-terminal measurements).

While two-terminal measurements are possible with each technique shown in Figure 2.1, three-terminal transport characterization is easier to achieve with nanofabricated devices (for instance, using a Si/SiO₂ chip with the highly doped silicon substrate acting as a backgate).

Of course, one should not forget that the choice of electrode material also plays an important role. The main requirements for the electrode material are: a slow oxidation rate, non-reactivity with solvents, high-atomic stability and accessibility. Based on these requirements noble metals are ideal materials for electrodes. However, high-atomic mobility of gold atoms at room temperature limits the usage of this material for electrodes at the nanometre scale. Platinum electrodes show a higher stability at room temperature, but thick metallic electrodes would cause screening of the gate in case of three-terminal measurements. Recent advances in material science brought two-dimensional layered materials into the field of nano-electronics. One of the most promising candidates for high-mobility electronic nanodevices is graphene. It is a conducting one-atomic-layer thin sheet of carbon atoms which are confined in a hexagonal honeycomb lattice. In this Thesis, we will show cases of using both platinum electrodes (Chapter 4) and graphene electrodes (Chapter 3).

2.3. NANO-OBJECTS AND THEIR NETWORKS

In Chapter 1 an overview over different types of nano-objects was introduced. Here, we describe in more detail three types of nano-objects (see Figure 2.6), which contain both organic and inorganic components and are the objects of study in this thesis. All three types of nano-objects listed in Figure 2.6 have a common inorganic unit – namely an iron ion(Fe). Iron is one of the most widespread metal in the world, and being incorporated into living species by binding to organic ligands it plays an important role in functioning of latter[23].

Metallo-proteins form an interesting class of metal-containing compounds[24, 25]. These proteins contain a metal-ion cofactor and their metal-binding sites are involved in important biological processes such as oxygen reduction, respiration, photosynthesis, nitrogen fixation, etc. In this thesis we explore the electrical properties of two proteins which contain transition metal ions – hemoglobin (Hb) and ferritin (Ft) (Chapter 5 and 6 respectively). Hemoglobin is an allosteric Fe(II) containing protein, stationed in the red blood cell (RBC). This protein consists of four subunits and each subunit contains a heme (a metal ion surrounded by a porphyrin ring) and a globin (polypeptide chains of amino acids) component. The functionality of hemoglobin comprises of oxygen uptake when saturated RBC travels from the lungs to a cell, and to transport carbon dioxide, a product of cell activity, from the cell back to the lungs. The size of Hb scales with the size of biological species it belongs to; for reference and in Chapter 5 we have taken the human protein with dimensions 5 nm x 4 nm x 5 nm. Cooperativity within its subunits is present when it binds and unbinds oxygen, i.e, when binding of a first oxygen molecule to one of the subunits occurs, other subunits within the protein become more acceptable for binding. The reverse process, oxygen unbinding, also follows this cooperativity effect.

Hybrid nano-objects

	Size* of nano-object	Metals in structure	Deposition methods
Spin-crossover nanoparticles (SCO NPs)	10 - 100 nm	Fe(II)	dielectrophoresis drop-casting
Hemoglobin (Hb)	5 nm	Fe(II)	drop-casting
Ferritin (Ft)	8 nm	Fe(III)	drop-casting

Figure 2.6: Hybrid nano-objects which contain Fe metal ions in their structure. *size = mean size in one of the three dimensions, typically the length. Nano-objects differ not only by size and deposition methods but also by their origin. SCO NPs can only be chemically synthesized, whereas haemoglobin and ferritin proteins originate from living organisms.

Ferritin is iron-containing protein which consists of 24 subunits. It contains iron in the Fe(III) state, which is incorporated in the mineral ferrihydrite and located inside the cavity. The main biological functions of this protein are iron storage and iron detoxification. Since ferritin is involved in important biological processes, a change in its concentration (or levels) may indicate deviation in normal functioning of the biological organism. For instance, elevation of ferritin in a brain tissue is one of the signals of Alzheimer's disease[26]. In Chapter 6 we study two types of ferritin obtained from hospital patients. The first is normal ferritin from healthy human beings, and the second one from patients with Alzheimer's disease. By measuring the electrical properties of these proteins, we show that it is possible to make a distinction between the two types of ferritin based on their conductance at the nano scale.

Another interesting class of compounds is spin-crossover nanoparticles (SCO NPs) known for their switching between low- and high-spin state at near room temperature[27]. Cooperativity between the metal centres of the SCO molecules within one nanoparticle result in thermal hysteresis, when the system switches between a diamagnetic (low-spin state) and a paramagnetic (high-spin state) state, triggered by a temperature change[28]. These properties make SCO NPs promising candidates for solid-state memory storage devices or molecular switches[29]. However, it has been shown that it is difficult to obtain reproducible hysteresis loops after several measurements, as the compound rapidly degrades in time in the presence of elevated temperatures. In Chapter 4 we investigate $[\text{Fe}(\text{Htrz})_2(\text{trz})(\text{H}_2\text{O})](\text{BF}_4)$ nanoparticles stabilized by SiO_2 shell, which presumably enhances stability of such compounds.

REFERENCES

- [1] Bumm, L. A., Arnold, J. J., Dunbar, T. D., Allara, D. L. and Weiss, P. S., *Electron Transfer through Organic Molecules.*, J. Phys. Chem. B **103**, 8122–8127 (1999).
- [2] Holmlin, R. E. et al., *Electron Transport through Thin Organic Films in Metal-Insulator-Metal Junctions Based on Self-Assembled Monolayers.*, J. Am. Chem. Soc. **123**, 5075–5085 (2001).
- [3] Tao, N. J., *Electron transport in molecular junctions.*, Nat. Nanotechnol. **1**, 173–181 (2006).
- [4] Kano, S., Tada, T. and Majima, Y., *Nanoparticle characterization based on STM and STS.*, Chem. Soc. Rev. **44**, 970–987 (2015).
- [5] Wold, D. J. and Frisbie, C. D., *Formation of Metal-Molecule-Metal Tunnel Junctions. Microcontacts to Alkanethiol Monolayers with a Conducting AFM Tip.*, J. Am. Chem. Soc. **122**, 2970–2971 (2000).
- [6] Reed, M. A., Zhou, C., Muller, C. J., Burgin, T. P. and Tour, J. M., *Conductance of a Molecular Junction.*, Science **278**, 252–254 (1997).
- [7] Moreland, J. and Ekin, J. W., *Electron tunneling experiments using Nb-Sn “break” junctions.*, J. Appl. Phys. **58**, 3888–3895 (1985).
- [8] Tans, S. J., Verschueren, A. R. M. and Dekker, C., *Room-temperature transistor based on a single carbon nanotube.*, Nature **393**, 49–52 (1998).
- [9] Park, H., Lim, A. K. L., Alivisatos, A. P., Park, J. and McEuen, P. L., *Fabrication of metallic electrodes with nanometer separation by electromigration.*, Appl. Phys. Lett. **75**, 301–303 (1999).
- [10] Ho, P. S. and Kwok, T., *Electromigration in metals.*, Rep. Prog. Phys. **52**, 301 (1989).
- [11] Black, J. R., *Electromigration: A brief survey and some recent results.*, IEEE Trans. Electron Devices **16**, 338–347 (1969).
- [12] Bolotin, K. I., Kuemmeth, F., Pasupathy, A. N. and Ralph, D. C., *Metal-nanoparticle single-electron transistors fabricated using electromigration.*, Appl. Phys. Lett. **84**, 3154–3156 (2004).
- [13] Qi, P. et al., *Miniature Organic Transistors with Carbon Nanotubes as Quasi-One-Dimensional Electrodes.*, J. Am. Chem. Soc. **126**, 11774–11775 (2004).
- [14] Wei, D. et al., *Real Time and in Situ Control of the Gap Size of Nanoelectrodes for Molecular Devices.*, Nano Lett. **8**, 1625–1630 (2008).
- [15] Prins, F. et al., *Room-Temperature Gating of Molecular Junctions Using Few-Layer Graphene Nanogap Electrodes.*, Nano Lett. **11**, 4607–4611 (2011).

- [16] Shi, S.-F., Xu, X., Ralph, D. C. and McEuen, P. L., *Plasmon Resonance in Individual Nanogap Electrodes Studied Using Graphene Nanoconstrictions as Photodetectors.*, Nano Lett. **11**, 1814–1818 (2011).
- [17] Nef, C. et al., *High-yield fabrication of nm-size gaps in monolayer CVD graphene.*, Nanoscale **6**, 7249–7254 (2014).
- [18] Island, J. O. et al., *Fabrication of hybrid molecular devices using multi-layer graphene break junctions.*, J. Phys. Condens. Matter **26**, 474205 (2014).
- [19] Grigorescu, A. E. and Hagen, C. W., *Resists for sub-20-nm electron beam lithography with a focus on HSQ: state of the art.*, Nanotechnology **20**, 292001 (2009).
- [20] Hu, W., Sarveswaran, K., Lieberman, M. and Bernstein, G. H., *Sub-10 nm electron beam lithography using cold development of poly (methylmethacrylate).*, J. Vac. Sci. Technol. B **22**, 1711–1716 (2004).
- [21] Rinaldi, R. et al., *A Protein-Based Three Terminal Electronic Device.*, Ann. N. Y. Acad. Sci. **1006**, 187–197 (2003).
- [22] Holovchenko, A. et al., *Near Room-Temperature Memory Devices Based on Hybrid Spin-Crossover@SiO₂ Nanoparticles Coupled to Single-Layer Graphene Nanoelectrodes.*, Adv. Mater. **28**, 7228–7233 (2016).
- [23] Beard, J. L., *Iron Biology in Immune Function, Muscle Metabolism and Neuronal Functioning.*, J. Nutr. **131**, 568S–580S (2001).
- [24] Finkelstein, J., *Metalloproteins.*, Nature **460**, 813–813 (2009).
- [25] Liu, J. et al., *Metalloproteins Containing Cytochrome, Iron–Sulfur, or Copper Redox Centers.*, Chem. Rev. **114**, 4366–4469 (2014).
- [26] Ayton, S., Faux, N. G. and Bush, A. I., *Ferritin levels in the cerebrospinal fluid predict Alzheimer's disease outcomes and are regulated by APOE.*, Nat. Commun. **6**, 6760 (2015).
- [27] Volatron, F. et al., *Spin-Crossover Coordination Nanoparticles.*, Inorg. Chem. **47**, 6584–6586 (2008).
- [28] Giménez-Marqués, M., García-Sanz de Larrea, M. L. and Coronado, E., *Unravelling the chemical design of spin-crossover nanoparticles based on iron(ii)–triazole coordination polymers. Towards a control of the spin transition.*, J. Mater. Chem. C Mater. Opt. Electron. Devices **3**, 7946–7953 (2015).
- [29] Bousseksou, A., Molnár, G., Salmon, L. and Nicolazzi, W., *Molecular spin crossover phenomenon: recent achievements and prospects.*, Chem. Soc. Rev. **40**, 3313–3335 (2011).

3

A FEW-LAYER GRAPHENE ELECTRODES FOR MOLECULAR ELECTRONICS DEVICES

In this chapter we report on the fabrication of a molecular transistor based on a single molecule trapped in few-layer graphene nanogap. The device is pre-patterned with Helium ion beam milling or oxygen plasma etching prior to nanogap formation. The nanogap is formed by applying high bias voltage between source and drain electrodes (electroburning) at room temperature. Pre-patterning helps to localize the gap, and to make it narrower, in the way that only a few or a single molecule can be trapped in the gap. In order to test the functionality of the device we deposited diamino-terphenyl molecule in the nanogap. Electrical measurements after deposition showed an increase of the current level as a function of the applied bias voltage.

3.1. INTRODUCTION

One of the open questions in molecular electronics is how to measure electron transport through a single molecule at ambient conditions. In order to do so, devices should possess certain requirements. First, the spacing between source and drain electrodes must be small enough to place a single molecule, which is typically of the order of a few nm. Up to now, several techniques such as mechanically controlled breakjunctions [1], nanolithography [2], electromigration [3] and others [4, 5] have been used to obtain nanoscale spacing between electrodes. A second important requirement is device stability at room temperature. Gold is the most common material for electrodes because of its noble character, but Au electrodes show instability at room temperature because of the high atomic mobility [6]. For this reason, most of the single-molecule measurements with gold electrodes are performed at cryogenic temperatures. Nevertheless operation at ambient temperature is crucial for future applications [7].

Graphene, a two-dimensional honeycomb lattice of carbon atoms shows exceptional electronic, mechanical and thermal properties that can be exploited for molecular electronics. Atomically thin graphene, or a few-layer graphene to avoid gating of the electrodes [8], can increase the gate coupling in molecular transistors, compared with bulky Au electrodes. Covalent binding of the carbon atoms in the lattice minimizes atomic mobility at room temperature resulting in stable electrode geometries. Also graphene enables a variety of anchoring groups that can be used for molecule attachment [9]. All these make few-layer graphene (FLG) a promising material for room temperature molecular devices.

In this chapter we show the fabrication approach for molecular three-terminal transistors using FLG flakes as electrodes, its electrical characterization before and after molecule deposition, and the detection of molecular transport.

3.2. DEVICE FABRICATION

3.2.1. NANOFABRICATION

The three-terminal transistors are fabricated on a heavily doped Si substrate coated with 285-nm thick SiO₂. The Si substrate is used as a common back-gate electrode. The surface is cleaned with ozone in order to minimize contamination and to maximize the adhesion of the flakes to the surface. FLG flakes are transferred onto the clean substrate by mechanical exfoliation using nitto tape. Suitable flakes [8] are selected by optical contrast under the microscope or by an AFM scanning. Two gold leads contact the graphene flake, as shown in the Figure 3.1, and are used for biasing the device.

The next step is to open the gap in FLG flake by using the electroburning technique (see 8 for more information) that allows to create a gap of a few nm. During electroburning the gap appears along the whole width of the flake, as seen in Figure 3.2, which is about 3 μm wide. The probability of having several molecules in the gap increases because of the micrometre width of the flake. Moreover, the gap may appear close to one of the gold electrodes resulting in the partial shielding of the gate voltage.

In order to overcome this issue a pre-patterning fabrication step is added prior to electroburning. The goal is to fabricate narrow FLG bridges. Two different approaches: 1) Electron-beam lithography (EBL) in combination with oxygen plasma etching (OPRIE), 2) He-ion beam (HIM) milling. Briefly, for the EBL approach the chip is covered

with a positive resist (PMMA) and exposed to the electron beam in such a way that the mask pattern for the etching is defined.

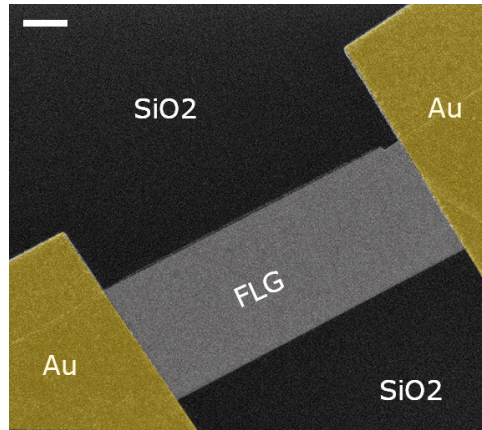


Figure 3.1: Scanning electron microscope (SEM) colored top view of the device after fabrication. The FLG flake is located between two Au electrodes on insulating SiO₂. Scale bar 500 nm

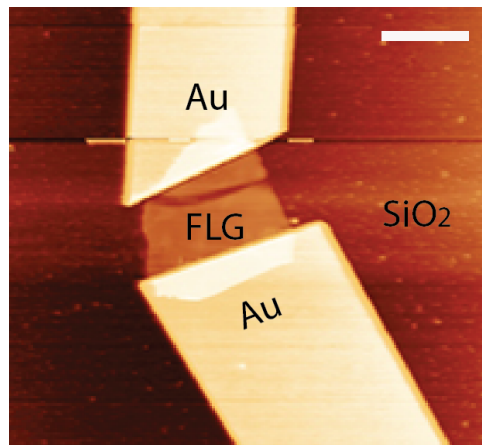


Figure 3.2: AFM image of a device after electroburning. The gap appears along the whole flake in close proximity to one of the electrodes, which may result in shielding of the gate field. Scale bar 2.5 μm .

Afterwards the resist is developed in MIBK:IPA (1:3) for 90 seconds and rinsed with IPA. Next, 1 min of the oxygen plasma etching is employed with a RF power of 20 W, a gas flow of 25 sccm O₂ and a pressure in the chamber of 50 μbar . In this step, the parts of the flakes that were not shielded by the resist are removed. The result is shown in the AFM image in Figure 3.3(a). Using this technique many devices can be processed simultaneously.

As an alternative to oxygen plasma etching, a He-ion beam microscope can be used. It is an universal nanofabrication tool that besides various applications [10–12] can per-

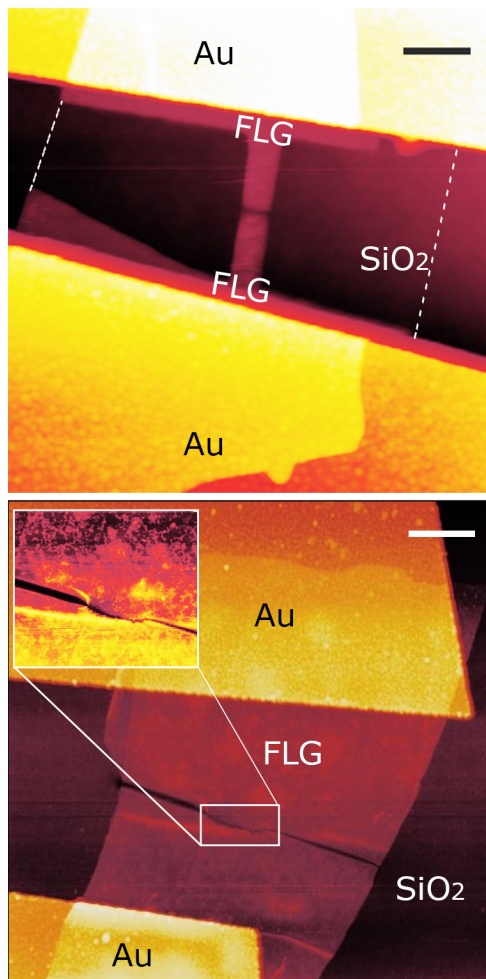


Figure 3.3: AFM image of a device pre-patterned with (top) combination of EBL and OP RIE. Scale bar 500 nm. (bottom) He-ion beam. After electroburning of pre-patterned device the nanogap appeared in the middle of the bridge. Inset: zoom in image of the junction. Scale bar 100 nm.

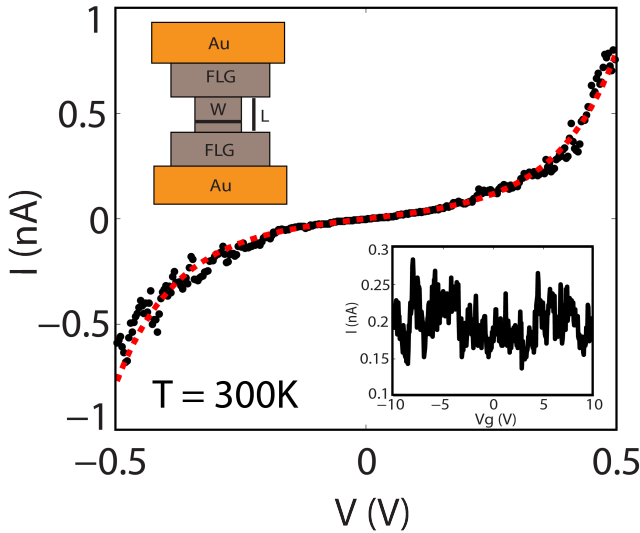


Figure 3.4: I-V characteristic of a pre-patterned device after electroburning. Bias voltage sweep $V_b = \pm 0.5V$ shows tunneling curve (black dots). The Simmons fit (dashed red line) is plotted on top along with the tunneling curve. Inset: Gate trace taken at $V = 0.3V$.

form ion-beam milling with nanometer resolution. The device is placed into the loading chamber of a Zeiss Orion HIM. The acceleration voltage for imaging is set to 25 kV in order to prevent charging effects on the surface of the chip. An internal pattern generator is used for pre-patterning, while the acceleration voltage in this case increases to 30 kV, enabling a beam current of 1 pA at a dose of 120 nC/cm. The patterned trenches, of about 10 nm wide, are narrower than with plasma etching, resulting in shorter bridges. For imaging after pre-patterning the acceleration voltage is reduced. A complete device is shown in Figure 3.3(b).

3.2.2. FEEDBACK-CONTROLLED ELECTROBURNING

After pre-patterning, feedback-controlled electroburning is used to create a nanoscale gap in the FLG flake. Electroburning is performed by ramping a high bias voltage (5 – 9 V) across flakes with initial resistances of kOhms and ohmic behavior in the current-voltage characteristics. At high current densities the flake heats up by the Joule effect and carbon atoms become mobile at the hottest areas in the pre-patterned channel. Feedback controlled software keeps track on the conductance of the device, and once it drops by 10%, the voltage is ramped back to the starting point (0.2 V), to prevent the uncontrollable breaking of the flake under high voltages. After ramping back, a new voltage sweep starts and the process is repeated until the device reaches a resistance in the range of GOhms, which indicates that a nanogap has been formed.

Figure 3.3 shows AFM images of electroburned devices that were pre-patterned with the two fabrication approaches mentioned above. The gap is opened in the center of the

bridge, thus realizing control over the localization of the nanogap formation.

Figure 4 presents the current while sweeping the bias voltage of a device after electroburning. The shape of this current-voltage characteristics resembles the one expected for single-barrier tunneling. The width of the gap can be estimated from a Simmons model (red dashed line in Figure 3.4). From the fit, with an area $A = 1100 \text{ nm}^2$ (width of the FLG bridge $W = 100 \text{ nm}$, length $L = 11 \text{ nm}$) we extract a barrier height $\phi = 0.6 \text{ eV}$ and a gap size $d = 2.2 \text{ nm}$. The inset in Figure 3.4 shows the current as a function of the applied back-gate voltage at $V = 0.3 \text{ V}$ at room temperature. The absence of gatedependent transport indicates that the gap is empty before molecular deposition. This observation combined with the small size of the gap makes the device suitable for molecular deposition and as a three-terminal molecular transistor.

3.3. ELECTRICAL CHARACTERIZATION AND MOLECULE DEPOSITION

To test the functionality of the fabricated devices we have performed deposition of diaminoterphenyl molecules on the electroburned FLG junctions.

1-Ethyl-3-(3-dimethylaminopropyl) carbodiimide (EDAC) has been used as a catalyst to form a covalent bonds between the NH_2 anchoring groups of the molecule and the carboxylic groups present at the edges of the gap. The chip with electroburned junctions was put in pyridine solution that contains a 1 mMol of terphenyl and 2 mMol of EDAC, and kept in this solution for 15 hours to let the molecules assemble on the surface and form the covalent N-C bonds in a chemical reaction. After taking the chip out from the solution it is dried naturally. At room temperature I-V measurements were performed. As Figure 3.5 shows, the current increases dramatically (red line) when compared to the current level before deposition (black line).

To characterize gate-dependent transport measurements were performed at 4 K. The gate sweep shown in Figure 3.6 taken at $V = 0.2 \text{ V}$ displays that the current is dependent on the gate voltage after the molecule deposition.

3.4. CONCLUSION

To conclude, we have studied the fabrication of nanogaps in pre-patterned FLG bridges using the electroburning technique. The pre-patterning of the flake enables localization of the gap, and reduces its length. To test the functionality of our device diamoterphenyl molecule has been deposited to the gap. The I-Vs after molecule deposition show an increase of the current level and gate dependence. These devices can be used to perform measurements on more complex molecules, or can be viewed as a first step towards more complicated molecular circuits involving more than one junction.

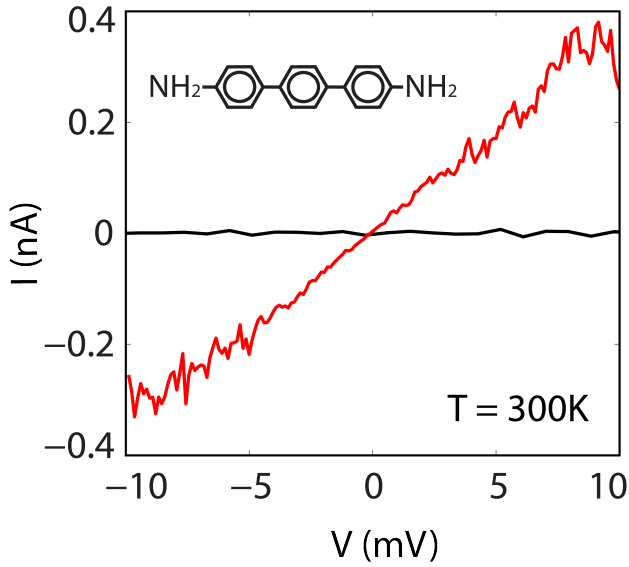


Figure 3.5: Current-voltage characteristic at room temperature of a FLG gap before (black line) and after (red line) molecule deposition.

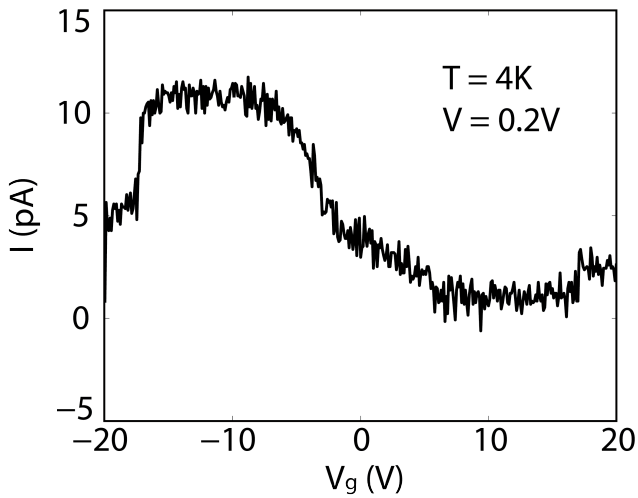


Figure 3.6: Current as a function of the applied gate after the deposition of 1mMol of terphenyl molecules. Measurements taken on a sample that is different from the one shown in Fig.5.

REFERENCES

- [1] J. M. van Ruitenbeek, A. Alvarez, I. Piñeyro, C. Grahmann, P. Joyez, M. H. Devoret, D. Esteve, and C. Urbina, *Adjustable nanofabricated atomic size contacts*, Review of Scientific Instruments **67**, 108–111 (1996).
- [2] M. D. Fischbein and M. Drndić, *Nanogaps by direct lithography for high-resolution imaging and electronic characterization of nanostructures*, APL **88**, 063116 (2006).
- [3] H. Park, A. K. L. Lim, A. P. Alivisatos, J. Park, and P. L. McEuen, *Fabrication of metallic electrodes with nanometer separation by electromigration*, APL **75**, 301–303 (1999).
- [4] H. M. Wang, Z. Zheng, Y. Y. Wang, J. J. Qiu, Z. B. Guo, Z. X. Shen, and T. Yu, *Fabrication of graphene nanogap with crystallographically matching edges and its electron emission properties*, APL **96**, 023106 (2010).
- [5] Y. He, H. Dong, T. Li, C. Wang, W. Shao, Y. Zhang, L. Jiang, and W. Hu, *Realization of size controllable graphene micro/nanogap with a micro/nanowire mask method for organic field-effect transistors*, APL **97**, 133301 (2010).
- [6] F. Prins, T. Hayashi, B. J. A. de V. van Steenwijk, B. Gao, E. A. Osorio, K. Muraki, and H. S. J. van der Zant, *Room-temperature stability of Pt nanogaps formed by self-breaking*, APL **94**, 123108 (2009).
- [7] E. Lörtscher, *Wiring molecules into circuits*, Nat Nano **8**, 381–384 (2013).
- [8] F. Prins, A. Barreiro, J.W. Ruitenberg, J.S. Seldenthuis, N. Aliaga-Alcalde, L.M. Vandersypen, H.S. van der Zant, *Room-temperature gating of molecular junctions using few-layer graphene nanogap electrodes*, Nano Lett. **11**, 4607 (2011).
- [9] P.D. M. Bodanszky, *Peptide Chemistry*, Springer Berlin Heidelberg, 1988.
- [10] M. C. Lemme, D. C. Bell, J. R. Williams, L. A. Stern, B. W. H. Baugher, P. Jarillo-Herrero, and C. M. Marcus, *Etching of graphene devices with a helium ion beam.*, ACS Nano **3**, 2674–2676 (2009).
- [11] S. A. Boden, Z. Moktadir, D. M. Bagnall, H. Mizuta, and H. N. Rutt, *Focused helium ion beam milling and deposition.*, Microelectronic Engineering **88**, 2452–2455 (2011).
- [12] D. C. Bell, M. C. Lemme, L. A. Stern, J. R. Williams, and C. M. Marcus, *Precision cutting and patterning of graphene with helium ions*, Microelectronic Engineering **20**, 455301 (2009).

4

MEMORY EFFECT IN SPIN-CROSSOVER NANOPARTICLES COUPLED TO SINGLE-LAYER GRAPHENE ELECTRODES

The charge transport properties of SCO [Fe(Htrz)₂(trz)](BF₄) NPs covered with a silica shell placed in between single-layer graphene electrodes are reported. A reproducible thermal hysteresis loop in the conductance above room-temperature is evidenced. This bistability combined with the versatility of graphene represents a promising scenario for a variety of technological applications but also for future sophisticated fundamental studies.

4.1. INTRODUCTION

In weak crystal fields octahedral complexes based on $3d^4$ – $3d^7$ transition-metal ions often display a spin-crossover (SCO)[1] between their high-spin (HS) and low-spin (LS) electronic configuration that can be induced by various external stimuli such as light, temperature, pressure, guest molecules, magnetic field and an electric field[2]. In addition, in the solid state some of these systems exhibit a remarkable memory effect as a result of strong cooperative elastic interactions occurring between metal centers[3].

In the last five years, several research groups have evidenced large memory effects in SCO devices by measuring their transport properties either in powdered samples[4–6] or in micro and nanostructures[7–10] going down to the single nanoparticle (NP) level[11]. Notably, the electrical control of the SCO has given an enormous impulse to this area,[11] and SCO NPs first reported by us in 2007[12], are nowadays considered as promising candidates to be used as active parts in molecular-based memory devices.

However, a practical use of these SCO devices has so far been hampered by the low reproducibility of the hysteresis loop in the conductance. This is particularly dramatic when one or a few NPs are contacted between electrodes for room-temperature (RT) operation[7, 11]. In fact, these devices rapidly degrade above RT and the thermal hysteresis loop often disappears after the first electrical-thermal cycle. To the best of our knowledge, the only example published of reproducible memory effect in the conductance at the nanoscale was demonstrated by us through 4 switches in the current-voltage characteristics operated at low temperatures (10 K) using $[\text{Fe}(\text{Htrz})_2(\text{trz})](\text{BF}_4)$ (Htrz = 1,2,4-triazole and trz = 1,2,4-triazolato) NPs coated with an organic surfactant[11]. Using interdigitated electrodes, Lefter et al.[9] measured up to 20 thermal hysteresis loops of the electrical current above RT for larger assemblies of organized micro-rods of the same SCO compound. However, even in these large assemblies a progressive degradation was systematically observed upon each thermal cycle (i.e. continuous current decrease). The loss of particle/particle or particle/electrode contacts may be the main cause of this electrical degradation, although one could imagine that the genuine fatigue of these compounds could be influenced in many other ways (temperature rate, voltage, intrinsic fatigue, etc.). In this line, a systematic diversification of both the probing techniques and physical conditions, as well as the nature and/or the range of the external stimuli applied should be considered to unveil and individually identify the mechanisms of fatigue.

In this context, graphene[13] may serve as an interesting new material for the electrodes. With only one atomic layer thin, graphene electrodes are non-invasive and conduct both heat and electricity very efficiently, while being at the same time thermally stable even above RT[14]. In addition, graphene is optically transparent and can efficiently guide surface plasmon modes that can be dynamically tuned by electrostatic gating[15]. The latter feature, in synergy with the memory effect in the dielectric properties of triazole-based SCO compounds[6] holds great promise to manipulate active plasmonic devices by an appropriate external perturbation[16]. All these characteristics make graphene a promising material to be used as electrodes in devices based on SCO NPs.

The coating layer, usually stabilizing sub-micrometric SCO NPs can also play a major role in their chemical stability, and thus in retaining memory-effect features. In particu-

lar, Mallah et al.[17] prepared hybrid SCO Fe(pyrazine)Pt(CN)₄ NPs using silica (SiO₂) as a robust inorganic shell; this methodology was later developed by Colacio et al. to form the hybrid [Fe(Htrz)₂(trz)](BF₄)@SiO₂ NPs[18, 19]. The latter hybrid core-shell NPs already proved to be multi-functional when decorated with luminescent molecules or gold NPs displaying both electronic bistability and luminescence[18, 19] or plasmonic[20] properties, respectively.

Recently, in a different approach the flexibility of conducting polymers (polypyrrole) has been reported to circumvent the problem of reproducibility. Galán-Mascarós et al.[21] prepared 50 μm-thick composite films made of similar triazole-based SCO compounds embedded in such conducting polymers. The conduction level of the latter turned out to be very sensitive to the thermally induced volume change of the SCO compounds, leading to a conduction change in a range of 50-300 %. However, this alternative strategy will become increasingly less suitable as device size decreases down to the nanometer regime, as strongly grafted conducting polymers on active SCO cores is not yet achieved.

In this chapter, we report the charge transport properties of SCO [Fe(Htrz)₂(trz)](BF₄) NPs covered with a silica shell placed in between single-layer graphene electrodes (i.e., enabling direct transport measurements). We evidence a reproducible thermal hysteresis loop in the conductance above room-temperature. This bistability combined with the versatility of graphene represents a promising scenario for a variety of technological applications but also for future sophisticated fundamental studies.

4.2. DEVICE FABRICATION AND NANOPARTICLE DEPOSITION

Graphene-based nanoelectrodes were fabricated on Si/SiO₂ substrates covered with commercially available CVD-grown single-layer graphene (obtained from Graphene Supermarket). First, gold leads were defined using e-beam lithography (EBPG5000Plus, PMMA resist, dose 900 μC / cm²), followed by metal evaporation (Leybold L560 evaporator) of Ti (5 nm) / Au (60 nm) and resist lift-off. Then, the surface was covered with PMMA resist and patterned with e-beam lithography to form an etch mask defining the graphene nanogaps with widths (W) ranging from 150-300 nm and lengths (L) in the 0.6-2 micron range (extracted from Scanning-Electron Microscope (SEM) images performed at an acceleration voltage of 15 kV). The unprotected areas were then etched away with oxygen plasma etching (Leybold Fluor etcher, 25 sccm, 20 W, 500 ubar) followed by resist lift-off.

Hybrid spin-crossover@SiO₂ NPs based on the system [Fe(Htrz)₂(trz)](BF₄), where Htrz = 1,2,4-triazole and trz = 1,2,4-triazolato, were prepared with the reverse micelle approach following a previously reported method with some modifications.[18] Two separate microemulsions containing the metal and ligand coordination polymer precursors with the silica precursor were first prepared. In the first microemulsion, an aqueous solution of Fe(BF₄)₂·6H₂O (337 mg, 1 mmol in 0.5 mL) and 0.1 mL of tetraethyl orthosilicate (TEOS) were added to a solution containing the surfactant Triton X-100 (1.8 mL), n-hexanol (1.8 mL) and cyclohexane (7.5 mL). A similar procedure was applied for the second microemulsion, comprising an aqueous solution of 1,2,4-1H-triazole (HTrz) (210 mg, 3 mmol in 0.5 mL). Both microemulsions were combined in air and the mixture was stirred to allow micellar exchange for 6 h. Finally, destabilization of the micelles upon addition of acetone promoted the precipitation of the NPs, which were then collected by

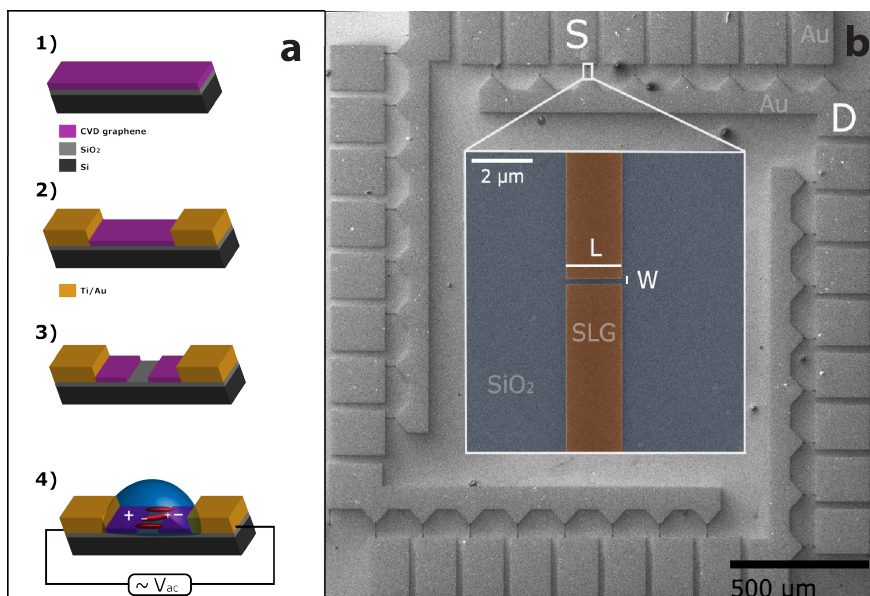


Figure 4.1: **(a)** Schematic of the fabrication process flow. Step 1-2: Gold contact pad and lead definition by electron-beam lithography, oxygen plasma etching and metal evaporation (see Experimental Section for more details). Step 3: Nanogap formation by electron-beam lithography and oxygen plasma etching. Step 4: Electrical trapping of the hybrid spin-crossover@SiO₂ NPs by a dielectrophoresis technique. **(b)** Scanning-electron microscopy micrograph of a chip before NP deposition containing 32 devices. Inset: Single-layer graphene electrodes of length $L = 1.7 \mu\text{m}$ and separation width $W = 300 \text{ nm}$ on a Si/SiO₂ substrate (false colour).

centrifugation at 12000 rpm, and washed several times with aliquots of EtOH (x3). TEM images were obtained from a JEOL JEM 1010 microscope (100 kV) and HRTEM images were collected with a Tecnai G2 F20 S-TWIN (200 kV). Sample preparation consisted on placing a drop of the NPs suspended in a solvent on a carbon coated copper grid.

A colloidal solution of the hybrid SCO@SiO₂ particles was obtained by diluting 5 mg of a powder in 5 ml of pure ethanol. This solution was diluted one hundred times. NPs were trapped in between the graphene electrodes using a dielectrophoresis method with the following parameters: 4 V peak-to-peak sine wave between source and drain at 10 kHz. SEM images were taken using a FEI Nova NanoSEM 450 microscope operating at 10 kV.

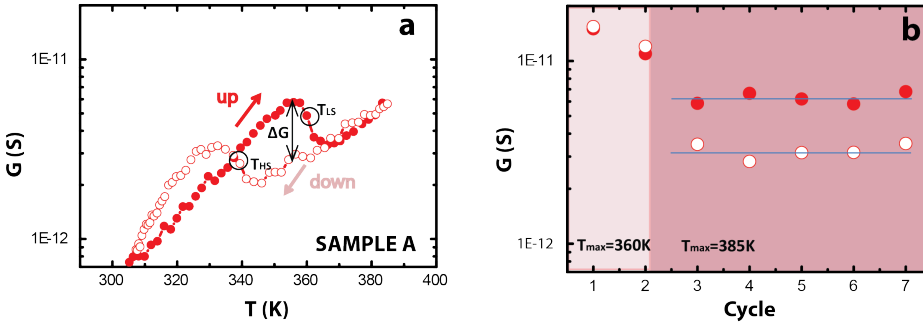


Figure 4.2: (a) Temperature-dependent conductance ($G = I/V$) measurements of sample A (cycle 6) showing hysteresis between the heating up (solid red circles) and cooling down (open white circles) cycle. (b) Conductance of sample A at $T = 350$ K and $V = 20$ V in the heating (solid red circles) and cooling (open white circles) modes for several cycles. Cycle 1-2: Maximum temperature while sweeping (heating mode) $T_{max} = 360$ K is too low for the spin switching to occur. Cycle 3-7: $T_{max} = 385$ K.

Sample	$L(\mu\text{m})$	$W(\text{nm})$	$\Delta G(\text{nS})$	$T^{LS}(\text{K})$	$T^{HS}(\text{K})$	$\Delta T(\text{K})$
A	1.7	150	2.18	340	360	20
B	0.7	250	5.88	340	374	33
C	1.7	300	6.11	335	374	39

Table 4.1: Poole-Frenkel parameters from four different devices (see also main text).

4.3. RESULTS

Single-layer graphene electrodes were defined with electron-beam lithography and oxygen plasma etching on commercially available Si/SiO₂/CVD-graphene substrates (see Figure 4.1(a) and Experimental Section for more details). Several combinations of the electrode-separation width to length ratios (W/L as defined in Figure 1.1(b)) were fabricated, enabling to contact a single NP with $L \approx W \approx$ the particle size, up to small assemblies of hybrid SCO NPs (representing a couple of NPs in series and about 30 possible parallel electrical pathways at maximum). A Scanning Electron Microscope (SEM) image of a representative device is shown in Figure 4.1(b).

Sample	$E_a^{LS}(\text{meV})$	$E_a^{HS}(\text{meV})$	$G_0^{LS}(\text{Sm}^{-1})$	$G_0^{HS}(\text{Sm}^{-1})$
A	417	295	5×10^{-6}	4×10^{-8}
B	1085	501	2×10^4	2×10^{-5}
C	887	464	56	1×10^{-5}

Table 4.2: Thermal activation energies (E_a) and pre-exponential factors (G_0) of the conductance in the two spin-states (HS – high spin state, LS – low spin state) for sample A, B and C. For parameter definitions see main text and Figure 3(a).

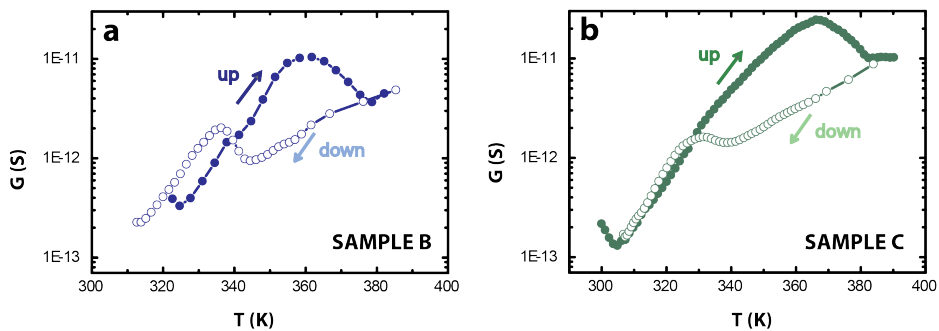


Figure 4.3: Conductance ($G = I/V$) as a function of temperature for (a) sample B at $V = 30$ V and (b) sample C at $V = 35$ V. Hysteretic behaviour of the conductance indicates NP switching between the low-spin state and high-spin state.

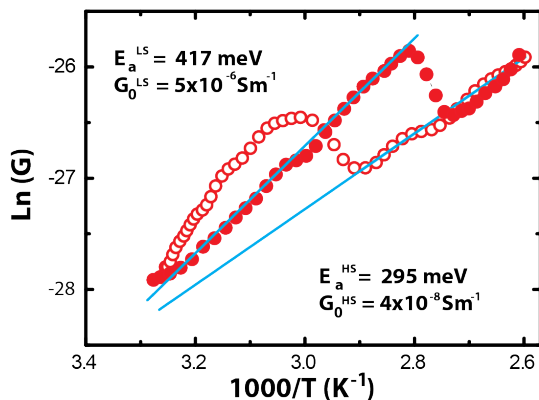


Figure 4.4: Arrhenius plot of the logarithm of the conductance vs. the inverse temperature of sample A. The activation energy is obtained by fitting a linear curve through the high-spin data (solid red circles) and the low-spin data (open white circles).

Core-shell SCO NPs of ca.110 nm in length and ca.50 nm in width were synthesized using published methods[18] (see Experimental Section and Figure 4.6 and Figure 4.7 for more details). The hybrid SCO NPs comprise a core of the $[\text{Fe}(\text{Htrz})_2(\text{trz})](\text{BF}_4)$ complex and a shell of SiO_2 . HRTEM has been carried out to provide structure details of the core/shell structure (see Figure 1.6). The shell thickness was about 11 nm for most particles, which is in good agreement with previous results[18]. The thermal spin-transition of the powder sample was magnetically established using a SQUID magnetometer (Figure 4.5). A suspension of the same powder was prepared in ethanol and drop-casted on top of the devices. A dielectrophoresis technique was used to trap the NPs in between the graphene electrodes (see Experimental Section for more details). SEM micrographs taken after deposition at an acceleration voltage of 10 kV show that in 85% of the devices (42 devices out of 49) few or even a single NP(s) was (were) placed between the two electrodes (see representative examples in Figure 4.7).

Electrical characterization of the devices was first performed before deposition. Current-voltage characteristics (I-Vs) were taken at atmospheric pressure using a cryostat probe station (Desert Cryogenics). All recorded I-V curves showed a maximum leakage current of about 5 pA while sweeping the bias voltage up to 35 V. Temperature-dependent conductance measurements before deposition showed no conductance change as a function of temperature between 305 K and 375 K (Figure 1.8). For these measurements a heater element was embedded in the probe station with a Lakeshore temperature controller and a local calibrated thermistor (TE-tech, MP-3011). Heating was performed at a rate of 2 K \cdot min $^{-1}$ by means of a resistor underneath the sample stage. Cooling was not done actively, but the rate could be controlled at high temperatures (from 385 K to 340 K), where the natural thermal dissipation exceeded 2 K \cdot min $^{-1}$ [22].

I-Vs recorded after deposition (same conditions as mentioned above) showed an increase of the current in 23 % of the devices (8 out of 34). These I-Vs are symmetric for positive and negative voltages and presented high voltage-activated current behaviors in good agreement with previous reports for polymer-coated SCO particles of the same family[7, 22] but also for surfactants-less microrods reported in the literature[7]. For these 8 devices, temperature-dependent conductance measurements were performed to investigate the spin-state dependence of the charge transport properties. It is important to note that the integrity of all graphene electrodes was preserved after deposition by dielectrophoresis method, as examined by SEM (see a representative example in Figure 4.7). The fact that the current levels of some of the nanogaps with NPs remained below our detection limit can be rationalized in terms of the size distribution of the cores and shells of the NPs randomizing the number of NP probed as well as the electrode coupling strength. It should also be noticed that an increase of current was only seen in the devices with a large W/L ratios. We observed no change in current after deposition for the devices, which have a W/L ratio equal to the size of the single NP. This could indicate that multiple parallel pathways are needed to observe a distinguishable current increase for these NP systems.

From SQUID measurements performed on a powder sample (see Figure 1.5) it is known that switching between the two spin states is expected in the temperature range from $T_{1/2}^{\uparrow} = 380$ K to $T_{1/2}^{\downarrow} = 340$ K ($T_{1/2}^{\uparrow}$ and $T_{1/2}^{\downarrow}$ = temperature for which there are 50 % of the Fe^{II} ions in the high-spin and 50 % in the low-spin states in the heating

and cooling mode, respectively). Figure 4.2(a) displays a thermal hysteresis loop in the conductance of the sample A ($W = 150 \text{ nm}$, $L = 1.7 \text{ }\mu\text{m}$) at an applied bias voltage $V = 20 \text{ V}$. The hysteretic behaviour of the conductance as a function of temperature is consistent with the temperatures observed in the powder sample.

Up to seven cycles (of sample A) were performed to check reproducibility of hysteresis features (Figure 4.2(b)). During the first two cycles the maximum temperature (T_{max}) was set to 360 K. Under these circumstances no conductance change between the heating and cooling modes was observed, indicating that 360 K is a too low temperature for spin switching to occur. When T_{max} was increased up to 385 K, a well-pronounced and reproducible hysteresis feature was observed (cycles 3-7 in Figure 4.2(b)). The conductance in the heating mode appears to be higher than in the cooling mode (open white and solid red circles, respectively). Importantly, for all five cycles the conductance values remain stable as well as the critical temperatures, which show that the spin switching does not degrade upon temperature cycling.

Figure 4.3(a) and (b) show the presence of hysteresis loops for sample B and sample C, respectively. These samples have a slightly different L/W ratio of the graphene electrodes, but the hysteresis behaviour remains a common feature of the data. Indeed, the critical temperatures for both the heating and cooling modes are very close for samples A, B and C and also in good agreement with the transition temperatures obtained on the powder sample (see Figure 4.5 for more information). Remarkably, the width of the hysteresis loop ΔT and the relative change in conductance ΔG are increasing with the separation width (W) of the graphene electrodes. Table 4.1 summarizes the parameters extracted from the hysteresis loops of the three devices (for sample A see Figure 4.2(a), for sample B see Figure 4.3(a) and sample C see Figure 4.3(b)). It is important to note, that the low-conducting state is the HS state for all three samples.

To compare relevant physical parameters, such as activation energy values (E_a) and pre-exponential factors (G_0) in both spin-states with those in the literature, we extracted these parameters from an Arrhenius fit through the data:

$$\ln G = \ln G_0 - (E_a / (k_B T)), \quad (1)$$

Note that we have used the conductance and not the conductivity in this equation, as we do not exactly know the current pathways in our samples.

The parameters obtained from the Arrhenius fits for sample A, B, C are given in the Table 4.2. One can note that for all three samples E_a and G_0 are both higher in the low-spin state compared to the high-spin state. Besides, the variation in the G_0 values is much larger (several orders of magnitude) than that in the E_a values.

In this chapter we demonstrated, for the first time, that graphene electrodes can be used to probe phase-transitions occurring near RT in SCO compounds. Dielectrophoresis deposition method[7] turned out to be an adequate method to position the small hybrid SCO@SiO₂ NPs in between the single-layer graphene electrodes. Importantly, we have observed reproducible hysteresis in the conductance upon thermal cycling for 5 times above RT. No degradation of the current levels has been detected, therefore we conclude that the robustness of the spin-transition after SiO₂ wrapping is significantly improved as compared with our previous results[11, 22] and with other reports[9].

As possible reasons influencing the spin-transition instability one can envision the following causes: i) a progressive breaking of the molecular structure induced by the thermal cycling, as shown recently by Grosjean et al., albeit not demonstrated at the nanoscale[23] ii) a modification in the charge of the metal centres/counter ions induced by the flow of charge carriers and/or sample environment[6, 24], iv) frictional forces at the NP/substrate interface[22, 25] or v) a loss of the electrical contact upon temperature cycles[9]. In distinguishing between these different reasons, the silica matrix could be beneficial as it decouples the active cores from the substrate and environment. Furthermore, the atomically thin graphene electrodes could yield an improved electrical contact with the hybrid NPs upon thermal cycles[14]. On the other hand, the intermediate size of the cores used in this work could delay or mask the intrinsic fatigue. Further studies are thus needed and in particular one should reproduce the same studies while scaling down the sizes of these hybrid NPs.

Another important observation is the spread of the hysteresis loop widths, which seems at a first glance in contradiction with recent results obtained on powder samples[19]. Indeed, our loop width value has increased to 19 K while using the same NP synthesis batch with lengths and widths respectively ranging from 107 ± 13 nm and 44 ± 10 nm. This contrasts with the recently reported work by Colacio et al., in which four syntheses of hybrid SCO@SiO₂ NPs of the same nature having very distinct lengths and widths ranging respectively between 56-422 nm and 56-180 nm, display hysteresis loop widths with variations of only 5 K. We ascribe this notable difference to the fact that we electrically probed only few NPs, whereas they used a SQUID magnetometer to magnetically characterise a large amount of material. Consequently, the changes in cooperativity due to different NP sizes, morphologies and silica thickness could be masked due to averaging.

As far as the transport mechanism in the SCO NPs is concerned, the Arrhenius fit to the data indicates a broad variation in the thermal activation energies and pre-exponential factors. A similar large spread was reported in the literature[26] associated to the different morphologies adopted by the same SCO compound, depending on the synthesis procedure. In contrast, the single-batch synthesis employed here points out that a large spread of pre-exponential factor and activation energies is already present and linked to the inherent core size distribution, silica shell thickness variation and/or local defects (structural and/or chemical)[4].

More importantly, we systematically found $E_a^{LS} > E_a^{HS}$ and $G_0^{LS} > G_0^{HS}$ while the opposite trend was reported for micro-rods made of the same SCO compounds that are not stabilized by a shell[4, 27]. Surprisingly, the low-conducting state (HS state) reported in this work remains, however, consistent with previous studies at the macro- and nanoscale[4, 6–10, 22, 27]. In this context, we speculate that the inversion in thermal activation energies and pre-exponential factors can be rationalized by the presence and the compression/relaxation of the silica shell accordingly to the expansion/relaxation of the NP cores upon SCO. Specifically, E_a and G_0 may originate from the contribution of hopping process mechanisms through both the core and the shell:

$$\ln G = \ln G^{\text{core}} + \ln G^{\text{shell}}, \quad (2)$$

where $E_a = E_a^{\text{core}} + E_a^{\text{shell}}$ and $G_0 = G_0^{\text{core}} \times G_0^{\text{shell}}$. Regarding the core contribution, it

has already been evoked that its pre-exponential factor G_0^{core} is governed by the competition of the product of the hopping distance and the hopping frequency[4]. Within the NP cores in the HS state, the well-known metal-ligand bond increase and softening will favour a charge carrier to hop further through the core, but with less probability. Similarly, we propose that the pre-exponential factor of the shell G_0^{shell} could be governed by the same competition, but yielding the opposite behavior. Within the shells in the HS, charge carriers will hop less far upon the silica compression but with higher probability.

Thermal hopping activation energies are even more complicated to capture[4], as it refers to the reorganization processes of atoms and molecules occurring for every charge transfer on SCO complexes. So far, higher activation energies have been reported consistently in the HS state for vast aggregates of nanometric particles[4] and micro-rods[27] made of the same SCO compound used in this work. One can interpret this result as the predominant role played by the distance accommodation between hopping sites compared to the energetical landscape upon SCO, but remain far from being understood. If higher activation energies of the NP cores in the HS state hold in our case, it means that the activation energy for the shells has to be smaller to explain the systematic conductance drop from our model in the HS state. This can be rationalized by the compression of the atoms distances within the shell in the HS state, which is expected to decrease the activation energy. These aforementioned intricate effects can thus explain an inversion of the activation energies and pre-exponential parameters compared to previous studies and points at the deformable ability of the silica shell wrapping the active cores.

One can wonder nevertheless, whether a tunnelling contribution within the shells can be expected for hybrid SCO@SiO₂ NPs as in the case of NPs stabilized by short organic polymers. Tunnelling transport occurs only if the barrier height is high and thin. In this line, HRTEM characterization of our SCO NPs reveals a silica shell thickness of 11 nm, and therefore the interparticle distances could be as large as 22 nm, which point at incoherent interparticle transport only. However, one cannot discard the presence of non-uniformities, defects or even pinholes across the SiO₂ shell leading to very thin tunnel barriers. Therefore, even though a incoherent interparticle transport mechanism is the most likely scenario in our work, coherent tunneling paths can not be totally excluded between hybrid NPs.

4.4. CONCLUSION

In this chapter we have successfully trapped small assemblies of hybrid SCO@SiO₂ NPs by a dielectrophoresis technique in between single-layer graphene nanogaps. This class of SCO NPs offers a large memory effect in the conductance of about 40 K associated with the spin-transition. The hysteresis occurs concomitantly with a reproducible and efficient back-relaxation to the low-spin state as a possible result of the enhanced stability provided by the silica shell on the SCO core NP. Moreover, the low-spin state possesses a higher conductance, consistent with previous studies on small assemblies of SCO-based NPs based on the same compound [Fe(Htrz)₂(trz)](BF₄). Importantly, the analysis of the hysteresis loop features points out that the presence of the silica shell can inverse the activation energies and pre-exponential factors while keeping the LS state as the high conducting state. We ascribe this feature to the compression(relaxation) of the shell in the HS(LS) state. The versatility of graphene combined with the thermal hysteresis loop

stability of the core-shell SCO NPs open up future experiments, such as injecting polarized spins and/or using the enhanced gate coupling to address the NP spin-state above RT and/or manipulate electromagnetic waves at the nanoscale.

4.5. APPENDIX

In Figure 2.5 we show magnetic measurements on SCO NPs powder described in this chapter. Figure 4.6 and 4.7 shows TEM and SEM images of the nanoparticles respectively. In Figure 2.8 the temperature cycle for a device before nanoparticle deposition is displayed. Figure 4.9 shows statistics over measured devices.

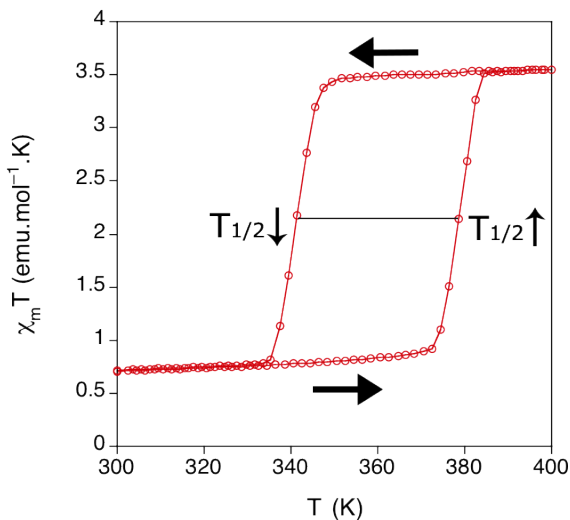


Figure 4.5: Temperature dependence of the molar magnetic susceptibility temperature product ($\chi_m \cdot T$) for powder samples of the hybrid spin-crossover $[\text{Fe}(\text{Htrz})_2(\text{trz})](\text{BF}_4)@\text{SiO}_2$ NPs after several heating-cooling modes.

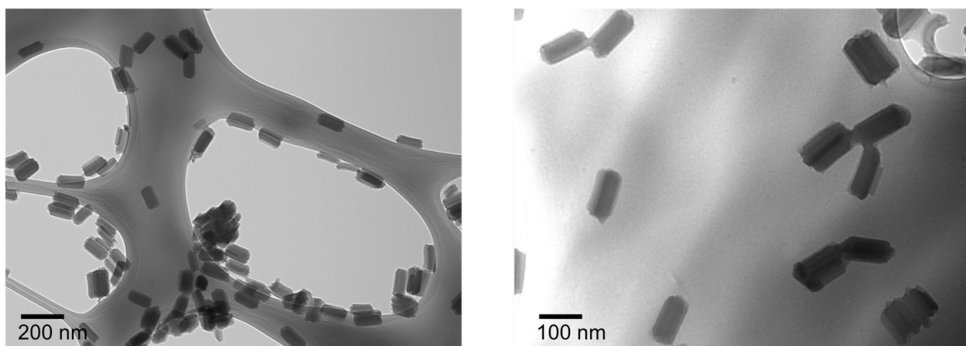


Figure 4.6: Transmission electron microscopy images of the hybrid SCO NPs deposited by drop casting on a carbon coated copper grid. Scale bars of 200 (left) and 100 nm (right).

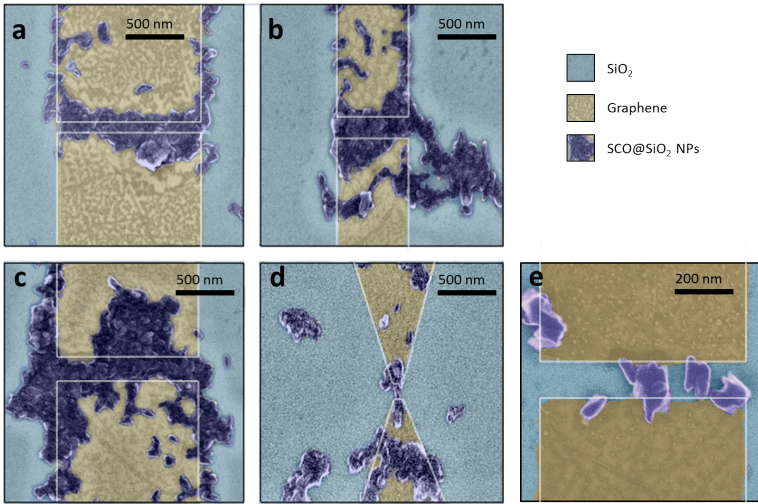


Figure 4.7: False colour scanning electron microscopy image of the devices after dielectrophoresis trapping. NPs were trapped in between graphene electrodes for (a) sample A (b) sample B (c) sample C (d) with triangular geometry ($W = 100$ nm, $L = 150$ nm) and (e) another sample provided by a lower filling factor which didn't exhibit a current increase after deposition. White lines indicate the position of the nanogap.

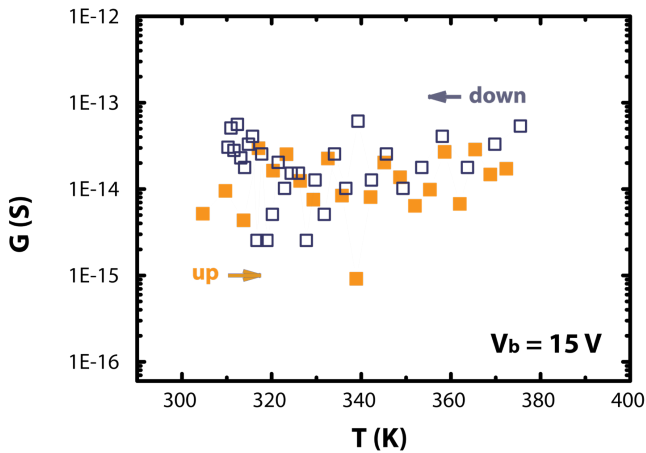


Figure 4.8: Conductance as a function of temperature for a device before NP deposition (heating mode: orange squares; cooling mode: blue empty squares). Notably, the conductance levels are orders of magnitude lower than the ones in the main text after NP deposition in particular around the hysteresis temperatures.

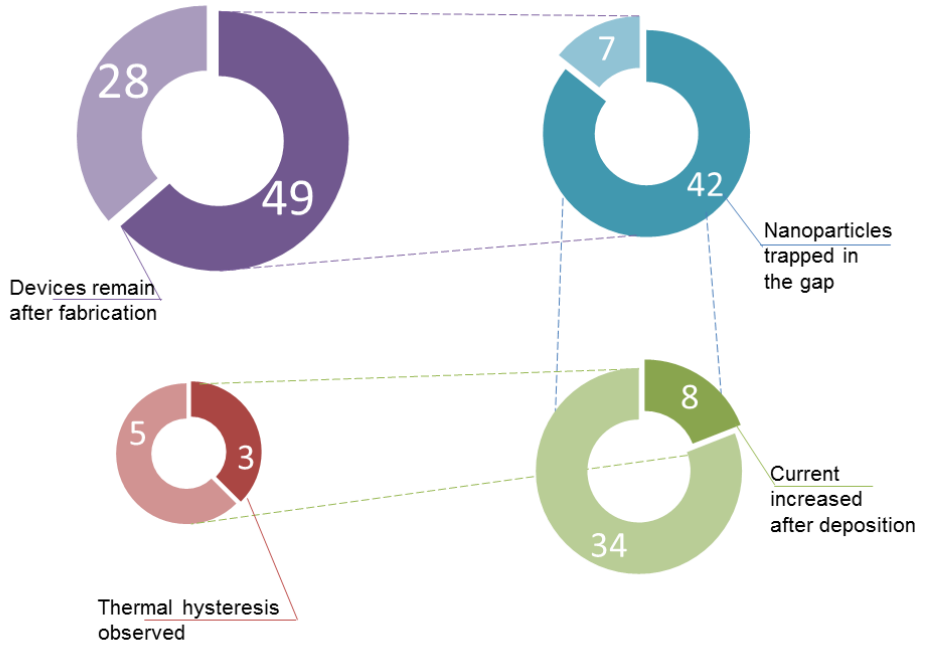


Figure 4.9: Statistics of: working/not-working devices remain after fabrication (purple chart), NP(s) trapped/not-trapped in the gaps (blue chart), electrical measurements after NP deposition (green chart) and thermal hysteresis observed in conductance (red chart).

REFERENCES

- [1] Gütlich, P., Hauser, A. and Spiering, H., *Thermal and Optical Switching of Iron(II) Complexes*, Angew. Chem. Int. Ed. Engl. **33**, 2024–2054 (1994).
- [2] E. Coronado, M. Giménez-Marqués, E. Mínguez Espallargas, F. Rey, I. J. Vitórica-Yrezábal, *Spin-Crossover Modification through Selective CO₂ Sorption*, J. Am. Chem. Soc. **135**, 15986–15989 (2013).
- [3] A. Bousseksou, G. Molnár, L. Salmon, W. Nicolazzi, *Molecular spin crossover phenomenon: recent achievements and prospects*, Chem. Soc. Rev. **40**, 3313–3335 (2011).
- [4] A. Rotaru, I. A. Gural'skiy, G. Molnár, L. Salmon, P. Demont, A. Bousseksou, *Spin state dependence of electrical conductivity of spin crossover materials*, Chem. Commun. **48**, 4163 (2012).
- [5] C. Lefter, S. Tricard, H. Peng, G. Molnár, L. Salmon, P. Demont, A. Rotaru, A. Bousseksou, *Metal Substitution Effects on the Charge Transport and Spin Crossover Properties of [Fe_{1-x}Zn_x(Htrz)₂(trz)](BF₄)(trz = Triazole)*, Phys. Chem. C **119**, 8522 (2015).
- [6] C. Lefter, I. A. Gural'skiy, H. Peng, G. Molnár, L. Salmon, A. Rotaru, A. Bousseksou, P. Demont, *Dielectric and charge transport properties of the spin crossover complex [Fe(Htrz)₂(trz)](BF₄)*, Phys. Status Solidi RRL – Rapid Res. Lett. **8**, 191 (2014).
- [7] A. Rotaru, J. Dugay, R. P. Tan, I. A. Gural'skiy, L. Salmon, P. Demont, J. Carrey, G. Molnár, M. Respaud, A. Bousseksou, *Nano-electromanipulation of Spin Crossover Nanorods: Towards Switchable Nanoelectronic Devices*, Adv. Mater. **25**, 1745 (2013).
- [8] C. Lefter, R. Tan, J. Dugay, S. Tricard, G. Molnár, L. Salmon, J. Carrey, A. Rotaru, A. Bousseksou, *Light induced modulation of charge transport phenomena across the bistability region in [Fe(Htrz)₂(trz)](BF₄) spin crossover micro-rods*, Phys. Chem. Chem. Phys. **17**, 5151 (2015).
- [9] C. Lefter, R. Tan, S. Tricard, J. Dugay, G. Molnár, L. Salmon, J. Carrey, A. Rotaru, A. Bousseksou, *On the stability of spin crossover materials: From bulk samples to electronic devices*, Polyhedron **102**, 434 (2015).
- [10] C. Lefter, R. Tan, J. Dugay, S. Tricard, G. Molnár, L. Salmon, J. Carrey, W. Nicolazzi, A. Rotaru, A. Bousseksou, *Unidirectional electric field-induced spin-state switching in spin crossover based microelectronic devices*, Chem. Phys. Lett. **138**, 644 (2016).
- [11] F. Prins, M. Monrabal-Capilla, E. A. Osorio, E. Coronado, H. S. J. van der Zant, *Room-Temperature Electrical Addressing of a Bistable Spin-Crossover Molecular System*, Chem. Phys. Lett. **23**, 1545 (2011).
- [12] E. Coronado, J. R. Galán-Mascarós, M. Monrabal-Capilla, J. García-Martínez, P. Pardo-Ibáñez, *Bistable Spin-Crossover Nanoparticles Showing Magnetic Thermal Hysteresis near Room Temperature*, Adv. Mater. **19**, 1359 (2007).

- [13] A. K. Geim, K. S. Novoselov, *The rise of graphene*, Nat. Mater. **6**, 183 (2007).
- [14] F. Prins, A. Barreiro, J. W. Ruitenbergh, J. S. Seldenthuis, N. Aliaga-Alcalde, L. M. K. Vandersypen, H. S. J. van der Zant, *Room-Temperature Gating of Molecular Junctions Using Few-Layer Graphene Nanogap Electrodes*, Nano Lett. **11**, 4607 (2011).
- [15] D. Rodrigo, O. Limaj, D. Janner, D. Etezadi, F. J. G. de Abajo, V. Pruneri, H. Altug, *Mid-infrared plasmonic biosensing with graphene*, Science **165**, 349 (2015).
- [16] K. Abdul-Kader, M. Lopes, C. Bartual-Murgui, O. Kraieva, E. M. Hernández, L. Salmon, W. Nicolazzi, F. Carcenac, C. Thibault, G. Molnár, A. Bousseksou, *Synergistic switching of plasmonic resonances and molecular spin states*, Nanoscale **5**, 5288 (2013).
- [17] Y. Raza, F. Volatron, S. Moldovan, O. Ersen, V. Huc, C. Martini, F. Brisset, A. Gloter, O. Stephan, A. Bousseksou, L. Catala, T. Mallah, *Matrix-dependent cooperativity in spin crossover Fe(pyrazine)Pt(CN)₄ nanoparticles*, Chem. Commun. **47**, 11501 (2011).
- [18] S. Titos-Padilla, J. M. Herrera, X.-W. Chen, J. J. Delgado, E. Colacio, *Bifunctional Hybrid SiO₂ Nanoparticles Showing Synergy between Core Spin Crossover and Shell Luminescence Properties*, Angew. Chem. Int. Ed. **50**, 3290 (2011).
- [19] J. M. Herrera, S. Titos-Padilla, S. J. A. Pope, I. Berlanga, F. Zamora, J. J. Delgado, K. V. Kamenev, X. Wang, A. Prescimone, E. K. Brechin, E. Colacio, *Studies on bifunctional Fe(II)-triazole spin crossover nanoparticles: time-dependent luminescence, surface grafting and the effect of a silica shell and hydrostatic pressure on the magnetic properties*, J. Mater. Chem. C **3**, 7819 (2015).
- [20] I. Suleimanov, J. S. Costa, G. Molnár, L. Salmon, A. Bousseksou, *The photo-thermal plasmonic effect in spin crossover@silica-gold nanocomposites*, Chem. Commun. **50**, 13015 (2014).
- [21] Y.-S. Koo, J. R. Galán-Mascarós, *Spin Crossover Probes Confer Multistability to Organic Conducting Polymers*, Adv. Mater. **26**, 6785 (2014).
- [22] J. Dugay, M. Giménez-Marqués, T. Kozlova, H. W. Zandbergen, E. Coronado, H. S. J. van der Zant, *Spin Switching in Electronic Devices Based on 2D Assemblies of Spin-Crossover Nanoparticles*, Adv. Mater. **27**, 1288 (2015).
- [23] A. Grosjean, N. Daro, S. Pechev, L. Moulet, C. Etrillard, G. Chastanet, P. Guionneau, *The Spin-Crossover Phenomenon at the Coherent-Domains Scale in 1D Polymeric Powders: Evidence for Structural Fatigability*, Eur. J. Inorg. Chem., 1961–1966 (2015).
- [24] C. Etrillard, V. Faramarzi, J.-F. Dayen, J.-F. Letard, B. Doudin, *Photoconduction in [Fe(Htrz)₂(trz)](BF₄)-H₂O nanocrystals*, Chem. Commun. **47**, 9663 (2011).
- [25] R. M. van der Veen, O.-H. Kwon, A. Tissot, A. Hauser, A. H. Zewail, *Single-nanoparticle phase transitions visualized by four-dimensional electron microscopy*, Nat. Chem. **5**, 395 (2013).

- [26] M. Giménez-Marqués, M. L. G.-S. de Larrea, E. Coronado, *Unravelling the chemical design of spin-crossover nanoparticles based on iron(II)–triazole coordination polymers: towards a control of the spin transition*, *J. Mater. Chem. C* **3**, 7946 (2015).
- [27] C. Lefter, S. Tricard, H. Peng, G. Molnár, L. Salmon, P. Demont, A. Rotaru, A. Bousseksou, *Metal Substitution Effects on the Charge Transport and Spin Crossover Properties of $[Fe_{1-x}Zn_x(Htrz)_2(trz)](BF_4)$ ($trz=Triazole$)*, *J. Phys. Chem. C* **119**, 8522 (2015).

5

ENVIRONMENT-DEPENDENT CONDUCTANCE MEASUREMENTS ON SOLID-STATE HEMOGLOBIN NETWORKS

We report on environment-dependant charge transport through hemoglobin networks, trapped in between platinum nanogaps with a 100-nm separation. The electrical measurements were performed while the environmental parameters (gas composition and pressure) were varied. We show that the current flowing through the hemoglobin networks is higher at ambient, suppressed in nitrogen gas atmosphere and not detectable in vacuum; the suppressed current is recovered by re-establishing ambient conditions. The Poole-Frenkel emission model is used to describe electron transport through the hemoglobin thin films with satisfactory agreement. The observed environment-dependent transport behaviour may be of interest for biosensor technologies.

In preparation for submission: A.Holovchenko and H.S.J. van der Zant "Environment-dependent conductance measurements on solid-state hemoglobin networks" (2017).

5.1. INTRODUCTION

Numerous studies on electronic properties and electron transport (ETp) through proteins[1] emerged in the field of bioelectronics. The attention to proteins is driven by the possibility of making bio-transistors and using proteins as an electronic material[2]. Besides, understanding of the electron transport mechanisms in proteins will give a better insight in their functioning and the electronic interaction between them. Among the different species, proteins with metallic co-factors (metalloproteins) are of a great interest[3, 4], because of the metal ions that are incorporated in protein polypeptide chains and may serve as sites for charges to hop on. Metalloproteins represent nearly half of all known proteins[5] and participate in essential biological processes, such as respiration, photosynthesis and redox reactions[6–8]. Multiple techniques have been employed to study the electrical conductivity of metalloproteins, ranging from using nanojunctions for contacting protein monolayers[9–11] to addressing a single protein molecule with Atomic Force Microscopy (AFM[12–14] or Scanning Tunnelling Microscopy (STM)[15, 16].

Hemoglobin (Hb) is an oxygen-binding allosteric protein present in the human body. The diameter of a single molecule is approximately 5 nm.[17] It consists of 4 sub-units (named 2-alpha and 2-beta), of which each has one Fe^{2+} coordinated to four pyrrol nitrogen atoms that fix the metal ion in a plane[18, 19]. The fifth binding site is in contact with a histidine amino acid, with one binding site available for the attachment of gas molecules (e.g. O_2 , CO, CO_2 or NO). Binding of a gas molecule causes a displacement of Fe^{2+} within the plane[20, 21], leading to significant structural changes in the protein - a characteristic known as cooperative binding[22]. The binding of a gas molecule to one sub-unit thereby increases the binding affinity of the neighbouring subunits.

Different approaches have been used to explore the electronic properties of hemoglobin. Hongxing Xu et al.[23] detected vibrational spectra of single hemoglobin protein molecules attached to 100-nm sized Ag nanoparticles. Earlier conductivity measurements on hemoglobin by B. Rosenberg[24] were made by placing proteins in between a metallic and a glass plate. The hemoglobin powder in this study showed semiconductor behaviour with a band gap of 2.3 eV. The influence of absorbed water on the conductance of a dry-state hemoglobin has also been reported.[25] Here, we report on electrical measurements in a planer on-chip configuration by contacting small assemblies of hemoglobin protein molecules with μm -sized platinum electrodes separated 100 nm apart. By applying a voltage between the source and drain electrodes we study the electrical properties of hemoglobin and monitor changes in the current as a reaction to the corresponding changes in the environment (e.g. pressure, temperature, gas composition).

5.2. EXPERIMENTAL SECTION

5.2.1. NANOFABRICATION

Devices are fabricated using a Si wafer with a 285 nm thick film of SiO_2 on top. The wafer is covered with a positive resist (PMMA) and exposed to an electron beam in a EBPG5000PLUS with a dose of $900 \mu\text{C}/\text{cm}^2$. The chromium/platinum contacts and electrodes have been created using thin-film metal evaporation (Leybold L560 evaporator) and resist lift-off in warm acetone. Scanning-Electron Microscope (SEM) imaging (FEI

Nova NanoSEM) has been performed at an acceleration voltage of 15 kV.

5.2.2. PROTEIN DEPOSITION

The solution with hemoglobin (Hb) is obtained by dissolving commercially available ferrous stabilized Hemoglobin A0 (supplier: Sigma-Aldrich) in DI water (electrical resistivity of 18 M ω -cm). Five mg of hemoglobin in powder form was mixed with 250 μ l of DI water, resulting in a concentration of proteins of 20 mg / ml. An aqueous solution containing the hemoglobin was then deposited onto the chip and placed in vacuum (5×10^{-3} mbar) to let the water to evaporate.

5.3. RESULTS

Electrodes were fabricated using standard e-beam lithography and metal evaporation; Figure 5.1a summarizes the fabrication process flow. The chromium/platinum (Cr/Pt, 3/40 nm thick) electrodes were evaporated onto a Si/SiO₂ wafer, coated with resist, and exposed to an electron beam. Figure 5.1b shows an example of a fabricated device with its dimensions: the lateral overlap between the two electrodes is 12 μ m and the spacing between them is approximately 100 nm. Subsequently, an aqueous solution of hemoglobin was drop-casted onto the patterned chip. Water was evaporated from the sample by placing the chip in vacuum. Scanning electron microscopy (SEM) images of the device before and after hemoglobin deposition are shown in Figure 5.1c and Figure 5.1d respectively. In this geometry approximately 20 hemoglobin proteins are thus connected in series. The number of proteins connected in parallel may vary between samples, as it depends on the hemoglobin coverage.

Current-voltage characteristics (I-Vs) were taken before (Figure 5.2a, black line) and after (Figure 5.2a, red line) deposition. All transport measurements were made at room temperature in a probe station. In Figure 5.2a the current levels after deposition appear to be significantly higher in comparison to those before the deposition. A clear conductance increase in 12 samples out of a total of 31 samples measured (Appendix Figure 5.10) was observed. Typical currents after deposition are of the order of a few hundred pA for a voltage of 10 - 15 V (Appendix Figure 5.11). In this paper, we discuss four representative sets of data taken on different samples.

Reproducibility of the current-voltage characteristics after deposition is shown in Figure 5.2b. Measurements of current over time were conducted whilst the voltage was swept back and forth in the range between -15 V and 15 V. Figure 5.2b displays five symmetric I-Vs that were recorded over a time frame of 45 min. Within this time frame, small variations in the current are found, but the overall shape of the I-V remains largely the same.

In Figure 5.3, the current flowing through sample A is plotted versus time at a fixed voltage ($V = 15$ V) applied under two different environments: air (blue regions) and vacuum (red regions). The current was first monitored in real time for a time of 6 minutes in air, as indicated by the green scale bar. Subsequently, air was pumped away from the chamber, establishing a pressure below $5 \cdot 10^{-3}$ mbar - the white space in the figure represents this part of the experiment. After pumping away the air, the recorded current dropped below 5 pA, which is the detection limit in our set-up. Over the course of the

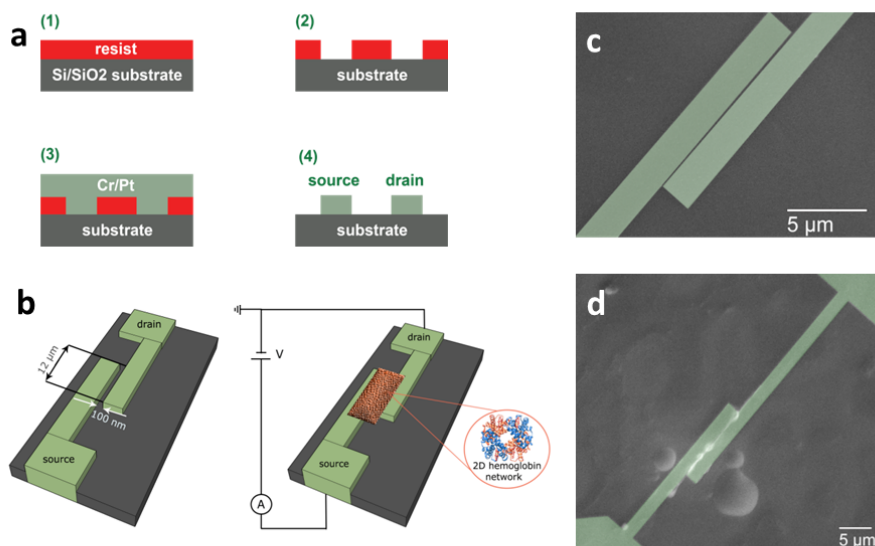


Figure 5.1: (a) Nanodevice fabrication schematic. Step 1-2: Resist pattern defined by electron-beam lithography. Step 3-4: Source and drain electrodes formed using 3 nm Cr/ 40 nm Pt metal evaporation and resist lift-off. (b) Hemoglobin network deposited onto the chip by a drop-casting method. (c) False-colour scanning-electron microscopy (SEM) image of the device before deposition and (d) after hemoglobin deposition. To facilitate SEM imaging the chip was covered with 3 nm of Au to reduce charging effects.

next 6 minutes the current remains low. Venting the chamber with atmospheric air results in a recovery of the current levels: when re-introducing air (second blue region) the current almost reaches its initial value. Moreover, current-voltage characteristics (left panel at the bottom) are similar to the ones shown in Figure 5.2b. Repeating the same pumping-venting sequence, the same behaviour is seen as shown in the right hand side of the main figure. In vacuum, the current is again below the noise level and after venting the I-V's (bottom panel on the right) recover to its initial state with similar current levels.

To further investigate the influence of the environment on the conductance, we have performed the same measurements but now instead of venting the system with air, it has been vented with atmospheric nitrogen gas. Figure 5.4 shows the current vs. time ($V = 15$ V) trace for sample B in the following media: air (blue regions), vacuum (red region) and nitrogen (white region). Probes were lifted up in the transition between air to vacuum or nitrogen. A similar behaviour as in sample A is observed for the air to vacuum transition – the current drops to below the detection limit upon reaching vacuum conditions. When venting the chamber with an atmospheric pressure of nitrogen gas, the current levels increase but do not restore to the initial level. In nitrogen, the current increases to about

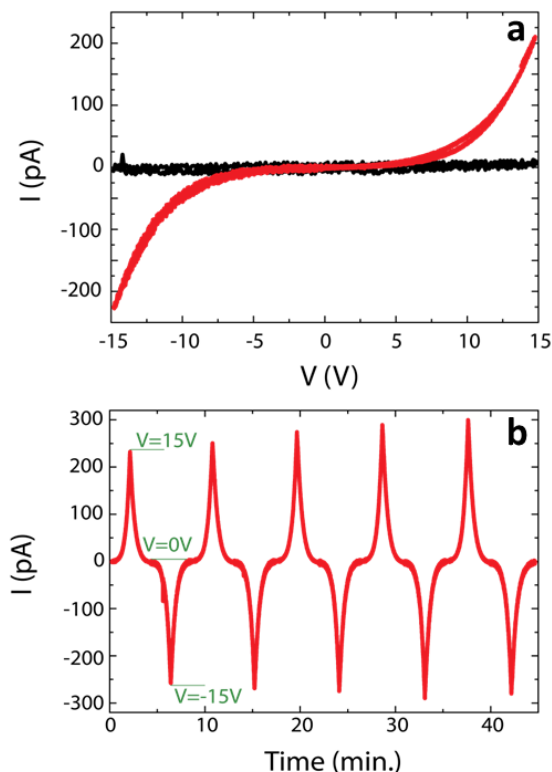


Figure 5.2: (a) Current-voltage characteristic of Sample A before (black line) and after (red line) hemoglobin deposition. After deposition an increase of the current is observed. (b) Five consecutive current-voltage sweeps show the stability of the current flowing through the device in time. Measurements taken at ambient conditions (room temperature, air) with a triangle sweep of the applied bias voltage with time.

1/3 of its initial value (see Figure 5.4, white region vs. blue regions). Only after replacing the pure nitrogen gas with air, the initial currents levels are reached.

Figure 5.5 displays a sequence of air to nitrogen transitions for sample C (a) and D (b). The transition between air and nitrogen was now recorded continuously. The current was recorded as a function of time, with the gas composition of the environment changing between air and nitrogen at ambient pressure.

The measurement started in air, followed by the introduction of the nitrogen gas to the chamber. A steep decay in current is observed in the presence of nitrogen gas. For both Sample C (Figure 5.5a) and Sample D (Figure 5.5b) the current is reduced by almost an order of magnitude, and suppressed to a value of 30 pA. After the air is introduced back into the chamber the current re-establishes its initial level.

We demonstrated that a small network of hemoglobin proteins can be contacted electrically by using 100-nm-spaced electrodes. The average current flowing through the protein network is in order of a few hundred pA. From sample to sample deviations in current (Appendix Figure 5.11) occur possibly due to a different number of proteins

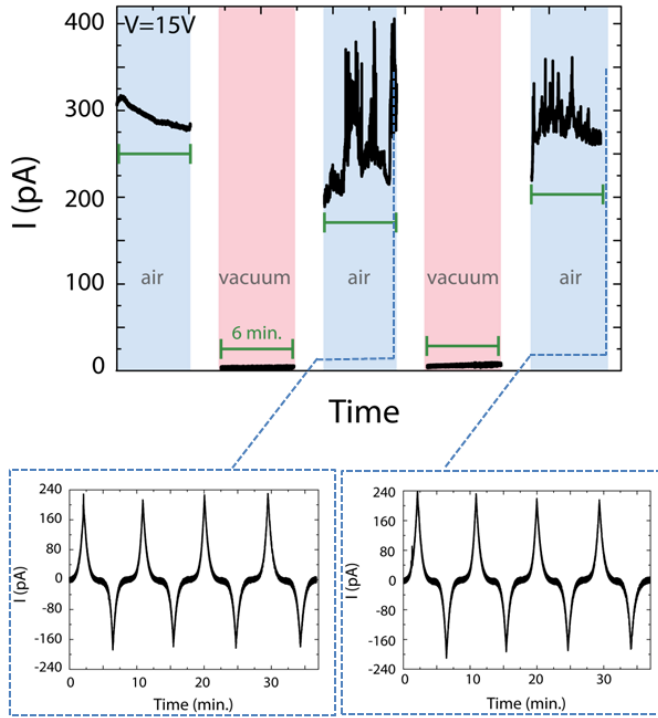


Figure 5.3: Current as a function of time for sample A at a fixed applied voltage ($V = 15\text{ V}$). A change in the current occurs as the sample goes from air (blue regions) to vacuum (red regions). The current drops to zero in vacuum and returns back to its initial value once it is in air again. Insets: current stability represented by four I-Vs recorded as a function of time while the voltage is swept linear between $\pm 15\text{ V}$.

being trapped within the gaps and the unpredictability of electrical pathways. Measurements furthermore show that the current is stable over time in the presence of both fixed or swept bias voltages at ambient conditions (Figure 5.2a and Figure 5.3 (blue regions) respectively).

To obtain more insight in the transport mechanism, the I-V curves were analysed in the context of the Poole-Frenkel (PF) emission model.[4, 26] This model describes field-enhanced thermal emission of charge carriers from traps and has been applied to characterize charge transport in thin dielectric materials, poorly conductive biological films and individual proteins.[26] In the PF model the current-voltage (I-V) dependence follows the law:

$$I = CV \exp\left[-q \frac{\phi_B - \sqrt{\frac{qV}{\pi d \epsilon_0 \epsilon_S}}}{kT}\right], \quad (1)$$

where q is the electron charge, d is the distance across which the voltage is applied,

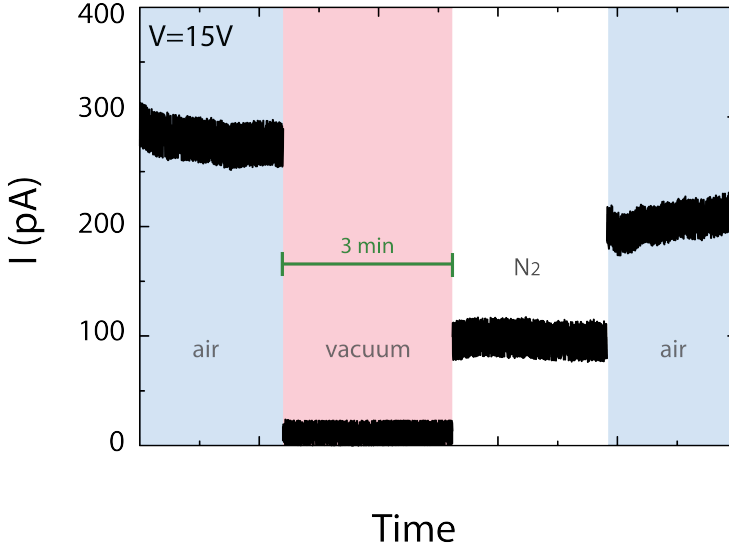


Figure 5.4: Current as a function of time at a fixed applied voltage ($V = 15$ V) for sample B. An environment-dependent change (similar to sample A) occurs while moving from air (blue region) to vacuum (red region). In nitrogen atmosphere (white region) a change in current occurs as well. The current levels are lower than in air, but above the noise level of 5pA.

ϕ_B is the energy barrier that an electron has to overcome in order to move between localized states, ϵ_s is the relative permeability of the material at high frequencies, ϵ_0 is the permittivity of free space, T is the absolute temperature, k is Boltzmann's constant, and C is a constant that depends on the effective area of the electric contact, the effective distance, bias voltage and on the intrinsic mobility of the charge carriers. The value of ϵ_s for hemoglobin depends on the hydration of the protein and may vary between 2.5 and 80.[27]

For two different samples the Poole-Frenkel plot for the I-Vs obtained for positive bias voltages is shown in the Figure 5.6. In this $\ln(I/V)$ vs. $V^{1/2}$ plot, the data points at high bias voltage were fitted to the model: reasonable linear fits can be obtained as indicated by the drawn red lines in this figure. The fit parameters are the intercept with the y-axis which is equal to $\ln C - (q\phi_B/kT)$ and the slope of the red lines (which we denote as b) which is $q/kT(\pi d\epsilon_0\epsilon_s)^{1/2}$

From the slope one can thus find the distance d as:

$$d^{1/2} = \frac{q^{3/2}}{BkT(\pi\epsilon_0\epsilon_s)^{1/2}}, \quad (2)$$

Table 1 summarizes the parameters for the two devices from the Figure 6 as well as the two other devices. The table shows that the value of the slope is about the same in all four samples, indicating that the product $d\epsilon_s$ is similar for these devices.[4] Because ϵ_s of the hemoglobin depends on the hydration of the protein which is in our case un-

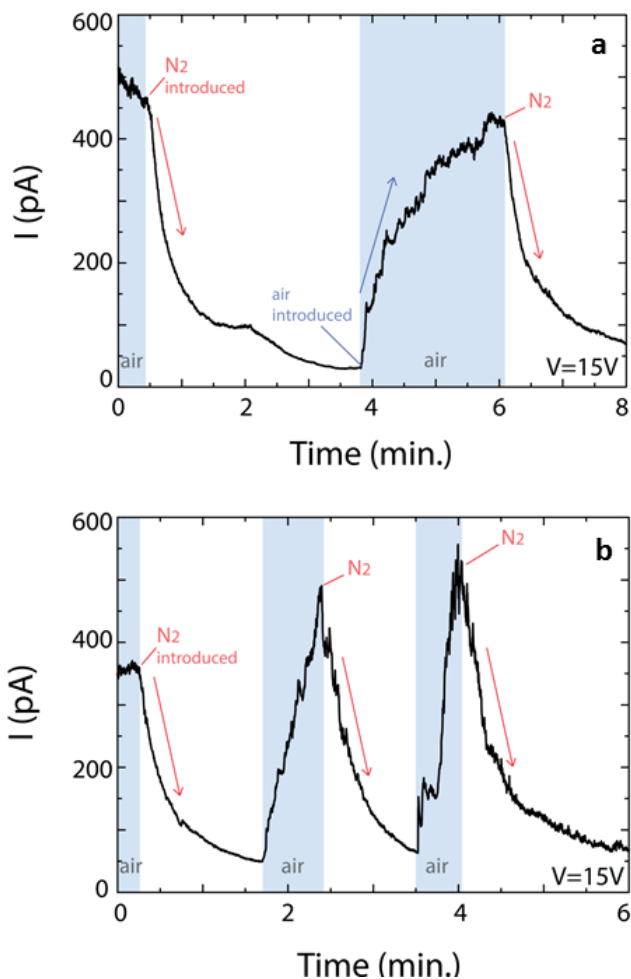


Figure 5.5: Current continuously monitored in time at a fixed applied voltage ($V = 15V$) for sample C (a) and D (b) at ambient pressure. (a) Current (black line) recorded as a function of time in air (first blue region). When nitrogen gas is introduced to the chamber, an abrupt drop in current is observed (first white region) similar to that of sample B. The decrease in current stops when air is introduced back to the chamber (second blue region), and decreases again in the presence of nitrogen gas (second white region). A similar trend is observed for sample D (b). Nitrogen suppresses the current flowing through proteins, with air recovering the current to its initial value.

known, we show two values of d : one for $\epsilon_s = 3$ (corresponding to a solid-state protein with almost no water molecules included) and one for $\epsilon_s = 80$ (highly hydrated protein). Values for d are then calculated to be in the range of tens of nanometre for the high ϵ_s value and approach the micron scale for the low $\epsilon_s = 3$. As the separation between the electrodes is 100 nm in all four cases, the comparison of the data to the model would thus suggest that one should take the high ϵ_s -value and that the proteins are thus highly

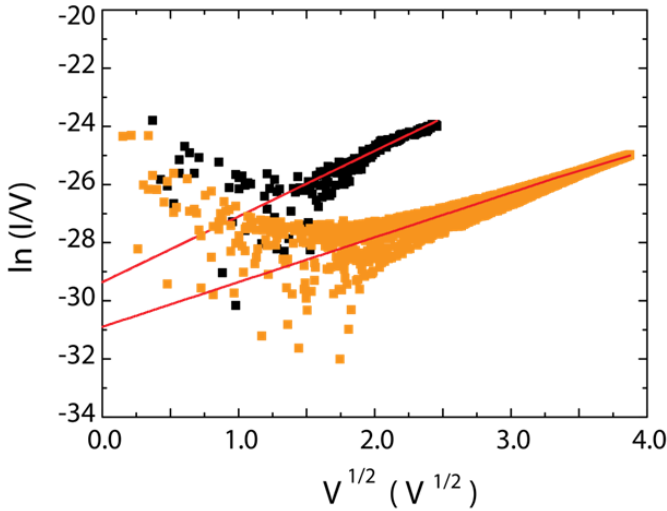


Figure 5.6: Poole-Frenkel plots for positive bias voltages for sample E (orange) and sample F (black). Drawn red lines are linear fits to the data. The scatter in the data at low bias reflects the noise in our setup. For sample F the maximum bias voltage is $V = 6$ V, for the sample E it is 15 V. I-Vs are taken at ambient and room temperature.

hydrated. In addition, the intercept for the four samples is also similar; the effective energy barrier which electrons have to overcome in order to escape from the trap ϕ_B should therefore be approximately the same in these samples. We thus conclude that the PF model provides a reasonable explanation to describe electron transport through the protein films but further investigation has to be done to come to a more firm conclusion. Further experiments could for instance be done as a function of temperature and see if the changes are in line with the prediction expected from PF emission. A change in current was observed when different environmental conditions were introduced. A higher current was detected in air, an order of magnitude lower current in atmospheric N_2 and no detectable current in vacuum. This trend was repeated in several samples across different batches. The strong environmental influence on hemoglobin conductance may be due to the impact of: i) gas pressure/concentration ii) gas composition or/and iii) the amount of absorbed water, remaining after the deposition or introduced by being in ambient conditions.

Let's consider the first the environmental conductance change from air to vacuum. In that case, the gas pressure in the chamber changes, while the gas composition remains the same. As a result of this transition, the monitored current through the device drops to below the detection limit range (less than 5pA). The same behaviour was observed for different samples and indicates that the gas pressure plays a prominent role in determining the current flowing through the protein network. The second transition, from air to nitrogen, was conducted at atmospheric pressure, but with a change in the gas composition of the chamber as the concentration of N_2 gradually increased. As a result, the current recorded as a function of time dropped almost an order of magnitude,

Sample	Slope($\ln(I/V)/V^{1/2}$)	Intercept ($\ln(I/V)$)	$d(\epsilon_s = 80)$	$d(\epsilon_s = 3)$
E	1.4	-30.5	$6.5 \times 10^{-8} \text{m}$	$1.6 \times 10^{-6} \text{m}$
F	2.3	-29.6	$2.2 \times 10^{-8} \text{m}$	$0.6 \times 10^{-6} \text{m}$
G	2.3	-31.4	$2.4 \times 10^{-8} \text{m}$	$0.6 \times 10^{-6} \text{m}$
H	3.1	-29.6	$1.2 \times 10^{-8} \text{m}$	$0.3 \times 10^{-6} \text{m}$

Table 5.1: Poole-Frenkel parameters from four different devices (see also main text).

suggesting that as in the first transition from air to vacuum air plays an important role in charge transport across protein networks.

It is already known that the Fe^{2+} metal ion in each subunit of hemoglobin has an affinity to bind oxygen, but the impact of this binding on electrical properties of the protein has yet to be proved. Our study shows that atmospheric air influences charge transport through hemoglobin and that the measured currents are higher in the presence of the air. However, it is not clear which component of the air contributes to this change the most. In our experiments, the current through the hemoglobin measured at ambient (20.9% O_2) was almost an order magnitude higher comparable to the one measured at N_2 atmosphere (lower O_2 concentration than in air) at ambient atmospheric pressure. This indicates that for higher protein conductance ambient conditions should be applied, and that a change in gas composition at ambient pressure will cause a decay in conductance. To ascertain the influence of gas composition on the conductance of hemoglobin networks further measurements with a control over gas concentration need to be performed.

From previous studies in bulk[24, 25], it is known that water can have a drastic impact on the conductance through hemoglobin. Ion-dominated transport, caused by the applied voltage is expected to be time dependent[25] in the absence of electrochemical reactions. In this paper, we studied current-voltage measurements that are stable over time. This indicates that the influence of water is not connected to the mobility of ions in it. The amount of water absorbed by the proteins could also affect the effective polarizability of the network. The change in the local dielectric environment influences the charge distribution in the protein network. It leads to a more effective screening and therefore to a lower barrier for hopping from one side to the next. It is unclear what the role of water is in our experiments, but since the vacuum conditions are quite mild (10^{-3} mbar at ambient, in which case the surface remains covered with a thin layer of water) and when changing the gas composition, experiments are performed at the same pressure, its role may be limited. More detailed studies are needed to ascribe the role of water in these kind of experiments.

5.4. CONCLUSION

In conclusion, we have reported on the electrical properties of sub-micron sized solid-state hemoglobin networks. Protein aggregates, trapped in between platinum nanoelectrodes, showed a stable electrical response while a voltage was applied across the nanogap at ambient. Our results provide evidence of environment-dependent current

flow through hemoglobin. The current dropped below the detection limit when vacuum conditions were set, and recovered to its initial value when the air was re-introduced. The presence of nitrogen gas in the chamber caused almost an order of magnitude drop in current. The environmental change in electrical response of hemoglobin networks suggests that it may be used in biosensor technologies. The advantage of the presented approach is that such sensor devices can be integrated on-chip with submicron-sized device dimensions.

5.5. APPENDIX

In Figure 5.7 a representative atomic force microscopy (AFM) image of sample A after deposition is shown. A white spot can be observed between the two platinum electrodes, with a profile that indicates 10 hemoglobin molecules in height.

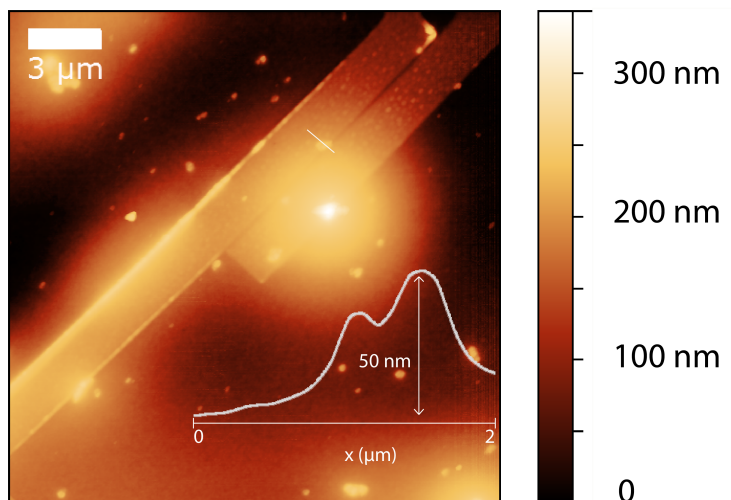


Figure 5.7: Atomic force microscopy (AFM) image of a device after hemoglobin deposition. The white line across the gap corresponds to the profile on the inset. The height of profile is 50 nm which corresponds to a film of 10 Hb proteins in height trapped within the gap.

Figure 5.8 shows an I-V characteristics of an empty device right after fabrication but before protein deposition. The current level is of the order of a few pA, which is the noise level of the measurements setup. This current level indicates that the nanogap is empty before the deposition. To verify that the solvent itself doesn't take an active part in charge transport I-V measurements were performed after deposition only solvent (without hemoglobin) (see Figure 5.9)). The current after solvent evaporation remained at the noise level, indicating that the nanogap is open.

In Figure 5.10 the statistics over the measured devices is shown. Approximately 36 percent of the devices show an increase in current after deposition. Remaining devices exhibited current levels of a few pA, the same as before deposition.

Figure 5.11 displays the current values of the 36 percent of the devices in which hemoglobin was trapped. The typical value of the current (at $V = 15$ V) is in the range of hundreds of pA.

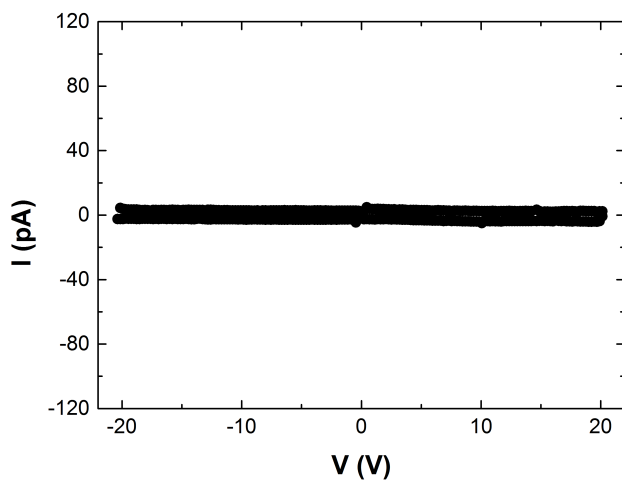


Figure 5.8: Current-voltage characteristic of (a) an empty device (without solvent or hemoglobin), and (b) after deposition of the dried out solvent (without hemoglobin), at ambient conditions. Current values in both cases are at the setup detection limit.

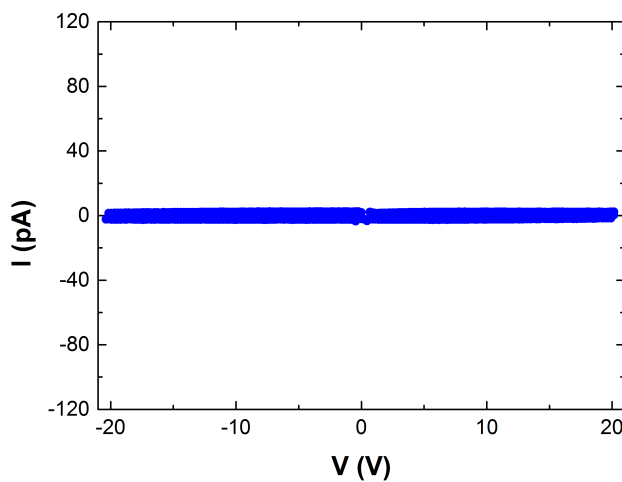
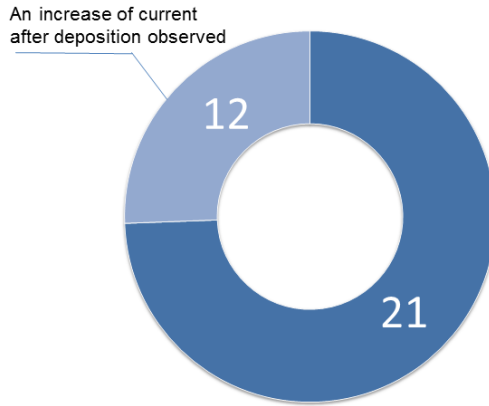


Figure 5.9: Current-voltage characteristic of (a) an empty device (without solvent or hemoglobin), and (b) after deposition of the dried out solvent (without hemoglobin), at ambient conditions. Current values in both cases are at the setup detection limit.



5

Figure 5.10: Statistics of devices that showed an increase of the current after deposition (12 devices, light blue chart) out of total number of devices fabricated (33 devices).

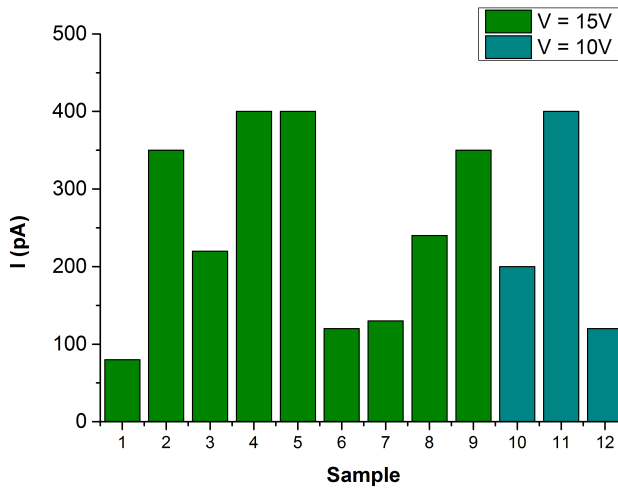


Figure 5.11: Maximum current value for the 12 different devices which showed an increase in current after deposition, determined at V = 15 V (9 samples, green bars) and V = 10 V (3 samples, blue bars).

REFERENCES

- [1] Blumberger, J., *Recent Advances in the Theory and Molecular Simulation of Biological Electron Transfer Reactions.*, Review of Scientific Instruments Chem. Rev. **115**, 11191–11238 (2015).
- [2] Willner, I. and Willner, B., *Biomaterials integrated with electronic elements: en route to bioelectronics.*, Trends Biotechnol. **19**, 222–230 (2001).
- [3] Raichlin, S., Pecht, I., Sheves, M. and Cahen, D., *Protein Electronic Conductors: Hemin–Substrate Bonding Dictates Transport Mechanism and Efficiency across Myoglobin.*, Angew. Chem. Int. Ed. **54**, 12379–12383 (2015).
- [4] Jett, J. E. et al., *Measurement of Electron Transfer through Cytochrome P450 Protein on Nanopillars and the Effect of Bound Substrates.*, J. Am. Chem. Soc. **135**, 3834–3840 (2013).
- [5] Waldron, K. J., Rutherford, J. C., Ford, D. and Robinson, N. J., *Metalloproteins and metal sensing.*, Nature **460**, 823–830 (2009).
- [6] Fedurco, M., *Redox reactions of heme-containing metalloproteins: dynamic effects of self-assembled monolayers on thermodynamics and kinetics of cytochrome c electron-transfer reactions.*, Coord. Chem. Rev. **209**, 263–331 (2000).
- [7] Armstrong, F. A., Heering, H. A. and Hirst, J., *Reaction of complex metalloproteins studied by protein-film voltammetry.*, Chem. Soc. Rev. **26**, 169–179 (1997).
- [8] Collman, J. P., Wagenknecht, P. S. and Hutchison, J. E., *Molecular Catalysts for Multi-electron Redox Reactions of Small Molecules: The ‘Cofacial Metalloporphyrin’ Approach.*, Angew. Chem. Int. Ed. Engl. **33**, 1537–1554 (1994).
- [9] Rinaldi, R., *A Protein-Based Three Terminal Electronic Device.*, Ann. N. Y. Acad. Sci. **1006**, 187–197 (2003).
- [10] Maruccio, G. et al., *Protein Conduction and Negative Differential Resistance in Large-Scale Nanojunction Arrays.*, Small **3**, 1184–1188 (2007).
- [11] Mentovich, E. D., Belgorodsky, B., Kalifa, I., Cohen, H. and Richter, S., *Large-Scale Fabrication of 4-nm-Channel Vertical Protein-Based Ambipolar Transistors.*, Nano Lett. **9**, 1296–1300 (2009).
- [12] Delfino, I. et al., *Yeast cytochrome c integrated with electronic elements: a nanoscopic and spectroscopic study down to single-molecule level.*, J. Phys. Condens. Matter **19**, 225009 (2007).
- [13] Xu, D., Watt, G. D., Harb, J. N. and Davis, R. C., *Electrical Conductivity of Ferritin Proteins by Conductive AFM.*, Nano Lett. **5**, 571–577 (2005).
- [14] Zhao, J., Davis, J. J., Sansom, M. S. P. and Hung, A., *Exploring the Electronic and Mechanical Properties of Protein Using Conducting Atomic Force Microscopy.*, J. Am. Chem. Soc. **126**, 5601–5609 (2004).

- [15] Friis, E. P. et al., *An approach to long-range electron transfer mechanisms in metallo-proteins: In situ scanning tunneling microscopy with submolecular resolution.*, Proc. Natl. Acad. Sci. **96**, 1379–1384 (1999).
- [16] Alessandrini, A., Corni, S. and Facci, P., *Unravelling single metalloprotein electron transfer by scanning probe techniques.*, Phys. Chem. Chem. Phys. **8**, 4383–4397 (2006).
- [17] Erickson, H. P., *Size and Shape of Protein Molecules at the Nanometer Level Determined by Sedimentation, Gel Filtration, and Electron Microscopy.*, Biol. Proced. Online **11**, 32–51 (2009).
- [18] Muirhead, H. and Perutz, M. F., *Structure Of Hæmoglobin: A Three-Dimensional Fourier Synthesis of Reduced Human Haemoglobin.*, Nature **199**, 633–638 (1963).
- [19] Schechter, A. N., *Hemoglobin research and the origins of molecular medicine.*, Blood **112**, 3927–3938 (2008).
- [20] Perutz, M. F., *Stereochemistry of cooperative effects in haemoglobin.*, Nature **228**, 726–739 (1970).
- [21] Baldwin, J. and Chothia, C., *Haemoglobin: the structural changes related to ligand binding and its allosteric mechanism.*, J. Mol. Biol. **129**, 175–220 (1979).
- [22] Ackers, G. K., Doyle, M. L., Myers, D. and Daugherty, M. A., *Molecular code for cooperativity in hemoglobin.*, Science **225**, 54–63 (1992).
- [23] Xu, H., Bjerneld, E. J., Käll, M. and Börjesson, L., *Spectroscopy of Single Hemoglobin Molecules by Surface Enhanced Raman Scattering.*, Phys. Rev. Lett. **83**, 4357–4360 (1999).
- [24] Rosenberg, B., *Electrical Conductivity of Proteins.*, Nature **193**, 364–365 (1962).
- [25] Rosenberg, B., *Electrical Conductivity of Proteins. II. Semiconduction in Crystalline Bovine Hemoglobin.*, J. Chem. Phys. **36**, 816–823 (1962).
- [26] Frenkel, J., *On Pre-Breakdown Phenomena in Insulators and Electronic Semiconductors.*, Phys. Rev. **54**, 647–648 (1938).
- [27] Pennock, B. E. and Schwan, H. P., *Further observations on the electrical properties of hemoglobin-bound water.*, J. Phys. Chem. **73**, 2600–2610 (1969).

6

TRANSPORT MEASUREMENTS ON ALZHEIMER'S FERRITIN NETWORKS

In this chapter we show that the distinction between pathological and physiological human ferritin can be made by means of conduction. The electrical measurements on both types of ferritin performed while the protein network is connected to platinum nanoelectrodes. We find that the current through Alzheimer's ferritin networks is lower comparable to physiological human ferritin.

6.1. INTRODUCTION

Ferritin is an iron-storage protein that can be found in a large variety of biological organisms[1] ranging from bacteria and fungi to animals. Non-covalent bonds hold the 24 polypeptide chains of ferritin together and form a hollow sphere with octahedral symmetry which can be loaded with iron atoms stored in a ferrihydrite form.[2, 3] Depending on the iron load there are several types of ferritin: the “iron-rich” form, known as holoferritin, contains up to 4500 iron atoms, and the “iron-free” form with no iron atoms is called apoferritin. While synthetic modifications can be applied to apoferritin to create a promising candidate for novel materials and drug delivery,[4] holoferritin has already been under scientific investigation because of its magnetic[5] and electrical[6–9] properties.

Considering the latter, the work of R. Davis[7] and co-workers focused on a conductance comparison between apo- and holoferritin in both monolayer protein films and single-ferritin molecules absorbed on a gold surface using conductive atomic force microscopy (CP-AFM). They concluded that polypeptide chains of ferritin act as a tunneling barrier, and that the conductance of holoferritin was higher than that of apoferritin. Another CP-AFM-based approach was presented by J. Davis[8] and co-workers. They studied and compared the conductance of individual ferritin particles and cytochrome c under different compression conditions. Modifications of the ferritin shell which undergoes compression changes in shape and size, lead to a change of the tunneling barrier. In case of apoferritin the shell compresses immediately, but holoferritin was found to be more robust and showed a linear increase in conductance while compressed due to the mineral core. Nijhuis and co-workers[9] investigated charge-transport regimes using ferritin as a model. In their work, a thin layer of ferritin was positioned in between a gold substrate and an EGaIn top-electrode. By performing temperature-dependent conductance measurements and changing the iron load of the protein layer, three types of tunneling regimes (single-step coherent tunneling, temperature-independent and temperature-dependent sequential tunneling) were observed, suggesting that the metal core of the ferritin plays an important role in long-range tunneling.

Besides iron storage, structural changes in ferritin act an indication of some severe diseases, such as Alzheimer's. It is known that iron atoms can catalyse free radical reactions that facilitate oxidation damage to the human brain. Recent research in the field of Alzheimer's disease (AD)[10] showed that in the presence of the apolipoprotein E the level of iron atoms in human body increases. Despite of enormous effort in this research area, the mechanisms which result in ferritin changes are still not well understood.

In this work we aim at detecting and distinguishing ferritin from healthy human beings and Alzheimer's human brain by means of electrical conductance measurements. In their native environment, these proteins are surrounded by dissolved electrolytes and ions, such as potassium and sodium which facilitate conductance in biological tissues. When performing electrical measurements in the “solid state” the impact of these cations on charge transport can be minimized. We demonstrate, that thin-film ferritin networks can be coupled to nanoelectrodes, and that the average conductance of Alzheimer's ferritin is about two orders of magnitude lower than that of physiological ferritin under the same conditions (temperature, pressure and applied voltage).

6.2. METHODS

Nanoelectrodes were fabricated on a silicon chip covered with a 285 nm thick layer of SiO₂. First, the chip was covered with resist (PMMA 950K) and spin-coat at 4500 rpm for 55 s and baked at 175 °C for 7 min.. The resulting layer thickness is about 140 nm. Subsequently, the device pattern was defined by using electron beam (e-beam) lithography (EBPG5000Plus, dose 900 $\mu\text{C} / \text{cm}^2$) followed by metal evaporation (Leybold L560 of Cr (5 nm) / Pt (45 nm)) and resist lift-off in hot acetone for 30 min.. A scanning electron microscope (SEM) image of a representative device is shown in Figure 1(a). The separation between the two electrodes is between 80-100 nm, which would allow to allocate 16-20 ferritin proteins in series. The human brain ferritin dissolved in a Phosphate buffered solution (PBS) was received from Leiden University (The Netherlands), and the protein preparation procedure is the same as described in the materials and methods section of Ref.[11]. The average particle diameter is 5 nm, and the concentration of the protein in PBS is 227.3 $\mu\text{g}/\text{ml}$ for Alzheimer's ferritin (AD Ft) and 210.5 $\mu\text{g}/\text{ml}$ for ferritin (Ft). Figure 1(b) shows a transmission electron microscopy (TEM) image of the human brain ferritin; the black dots represent the ferritin cores.

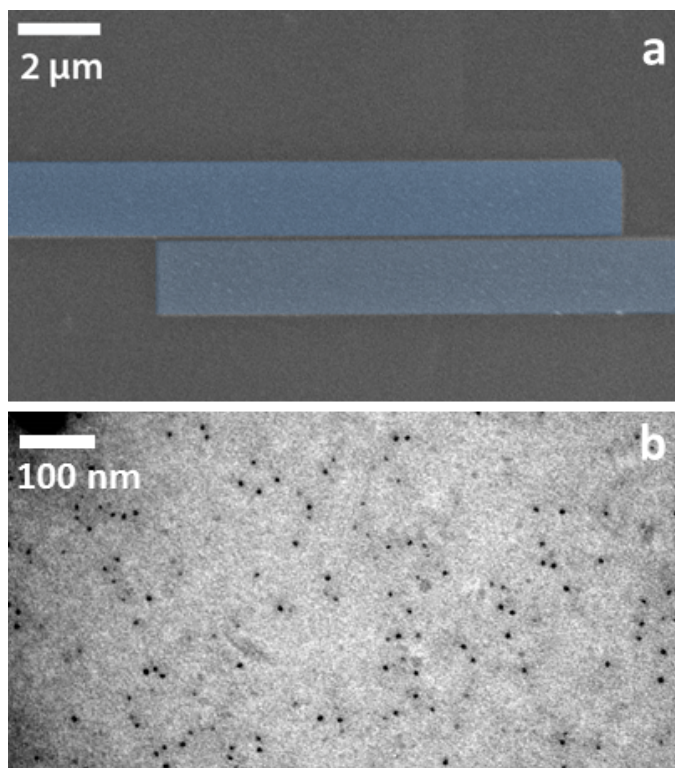


Figure 6.1: (a) Scanning electron microscopy (SEM) image (false colour) of a pair of platinum nanoelectrodes. Separation between the electrodes is 80 nm. (b) Transmission electron microscopy (TEM) image of a ferritin solution deposited on a TEM grid.

6.3. RESULTS AND DISCUSSION

Devices were electrically characterized before and after the deposition of the proteins. Current-voltage (I-V) characteristics were recorded by applying a voltage across the electrode pair and measuring the current flowing through the device. In the two chips investigated 26% (7 devices) were shorted after fabrication, indicating that some residuals remained in the gap between the two the electrodes causing an electrical connection between them; these junctions are disregarded in the remainder. The other junctions show an open circuit and these are used for the electrical characterization of the protein networks. More details about the statistics can be found in Figure 2.

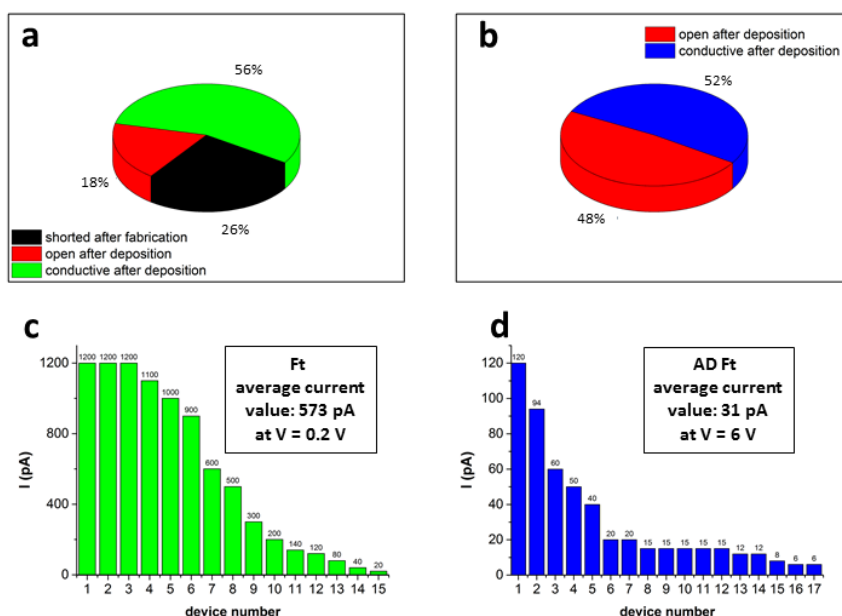


Figure 6.2: Statistics over the samples that showed an increase in the current after deposition for (a) ferritin (Ft) (b) Alzheimer's ferritin (AD Ft). Values of the current at $|V| = 0.2$ V for the devices with Ft (c), and the values of current at $|V| = 6$ V for the devices with AD Ft (d). Note, that for ChipB no shorted devices were found after fabrication

After the electrical check before deposition, a solution with ferritin (Ft) and Alzheimer's ferritin (AD Ft) was applied onto Chip A and Chip B respectively. The yield of the junctions that show an increase in current for Chip A is 56% and for Chip B it is 52% (see Figure 2(a) and (b) respectively). Representative current-voltage (I-V) characteristics are displayed in Figure 3(a) for Ft and in Figure 3(b) for AD Ft. The asymmetry in the I-V's may come from the fact that the coupling of the protein thin film to one of the electrodes is stronger than to the other one. Noticeably, a markedly different voltage has to be applied across the networks with the two types of ferritin to reach the same current; the device with Ft is more conductive than the one with AD Ft. To confirm that this is a systematic trend, we show in Figure 3 (c) and (d) the statistics of current values on all

devices across the chips, calculated as the average value of the current at a fixed negative and positive bias voltage value. From Figure 2(c) we find that the average current value for Ft over 15 devices is 573 pA at $|V| = 0.2$ V, and from the Figure 2(d) this value is 31 pA at $|V| = 6$ V for AD-Ft obtained as an average over 17 devices. Thus, the samples with Ft are systematically more conductive than AD Ft those containing. In Figure SI 1 several I-Vs of devices with Ft and AD Ft up to the same maximum applied voltage ($V = 4$ V) are shown. As in case of the data displayed in Figure 2, the current through Ft remains higher in comparison to the current of the AD Ft samples.

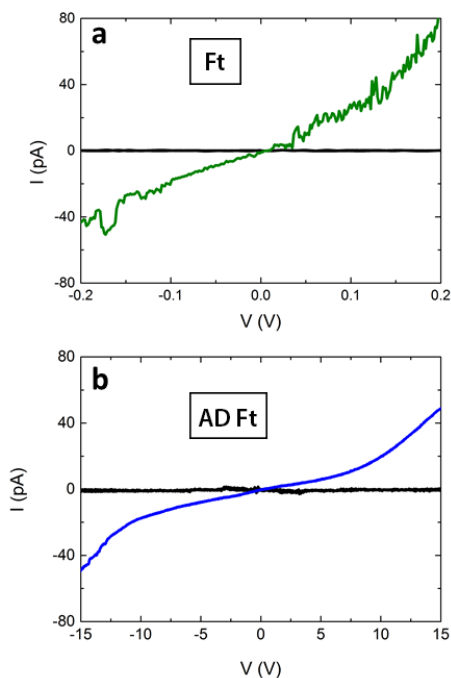


Figure 6.3: Current-voltage (I-V) characteristics of (a) ChipA_14 before (black line) and after deposition (green line) of human ferritin (Ft). An increase of current after deposition is observed, which indicates that charge carriers are passing through the deposited proteins. (b) I-V for ChipB_12 with Alzheimer's (AD Ft) human ferritin (blue line). Similar to (a), the current increases after protein deposition, but the Ft network is much more conductive than the one containing AD Ft, as for reaching the pA range current the applied voltage in the former case is about two orders of magnitude smaller to be applied across the sample with Ft.

To check the stability of the measurements, we have recorded consecutive IV's over a period of over 15 min.. Figure SI 2 shows the I-V of ChipA_13 after protein deposition. The inset of this figure contains the reproducibility measurement, which consist of four consecutive I-Vs recorded while the voltage was swept between -4 and 4 V. We further note that the asymmetry remains the same for these four I-Vs, indicating that it is a reproducible feature of this sample.

The influence of the environment on the electrical properties of the Ft and AD Ft networks was addressed by changing the gas composition of the chamber from air to pure

nitrogen gas. In Figure 4 (a) the current as a function of time at a fixed applied voltage of $V = 4$ V for Ft sample (ChipA_15) is displayed. The recording of current starts in air showing small fluctuations in the current around 150 pA. Once nitrogen gas is introduced in the chamber the current decays and reaches the detection limit of our setup. However, when air is pumped back into the chamber, the current level re-establishes itself and in this case almost doubles its value compared to the starting point before the nitrogen exchange. The same trend was observed for samples with AD Ft. Because of the detection limit of the setup (5 pA) and the relatively low conductance of AD Ft (tens of pA at $V = 6$ V, see Figure 2 (d)) higher voltages ($V = 15$ V) were applied across the AD-Ft samples to record a detectable signal (see Figure 1.4b). A similar experiment but with oxygen gas exchange has also been performed; for sample ChipA_15 the results are shown in Figure 6.8. Just as in the case of nitrogen, oxygen introduced in the chamber causes a suppression of the current. But unlike with nitrogen, in which case the current decays to the noise level of the setup, the current recorded in the presence of oxygen dropped to 110 pA and remained there. From the experiment described above we thus conclude that the current of both Ft and AD Ft networks is dependent on the gas composition of the environment, and in the case of gas exchange can be re-established back to its approximately initial value by returning to ambient conditions.

In this paper we demonstrated, that the electrical properties of human brain Alzheimer's ferritin (AD Ft) are different from reference samples containing ferritin (Ft). The ferritin was coupled to platinum nanoelectrodes with a separation of 80-100 nm. Reproducible electrical measurements were obtained for both types of the protein. Importantly, the AD Ft appeared to be systematically less conductive than the Ft, which may originate from structural differences of the protein's shell or/and core. Ferritin itself consists of 24 subunits: a light (L) and heavy (H) type that are co-assembled in a heteropolymeric shell. The H-chain subunit is known to be a ferroxidase and catalyses the oxidation of Fe(II) to Fe(III), whereas L-chains take part in electron transfer during mineralization and demineralization processes.[12, 13] The ratio between the H and L chains is tissue-specific but it can be modified in the presence of degenerative diseases, such as Alzheimer's. The reports by Fleming and Joshi[14] and by P.Harrison[15] and co-workers show that the ferritin from Alzheimer's patients have an H-subunit content of 70%, resulting in inefficient iron nucleation inside the ferritin cavity. Since the ratio between L and H units (70:30%) in AD Ft is different from physiological ferritin, a lower conductance of this protein may mean that electron transport, in the case it occurs through the shell of the protein, is dependent on the amount of L units.

If not the shell but the core dominates charge transport, one should consider the difference in either the number of atoms or its oxidation state. Physiological ferritin has an Fe(III) oxide core (ferrihydrite with 20% FeO₄ and 80% FeO₆), whereas pathological AD ferritin has a ferric-ferrous (Fe(II)-Fe(III)) iron oxide (magnetite) core. Dominguez-Vera and co-workers[16] used different inspection techniques (TEM, SAXS, XANES, EELS, and SQUID) for systematic studies of the ferritin core. They showed that it consists of three phases (hematite, magnetite and ferrihydrite) and that the proportion of each phase changes with respect to a change in iron filling of the core. Also, magnetic measurements showed that the magnetite phase becomes dominant only when the iron content drops below 500 Fe atoms.

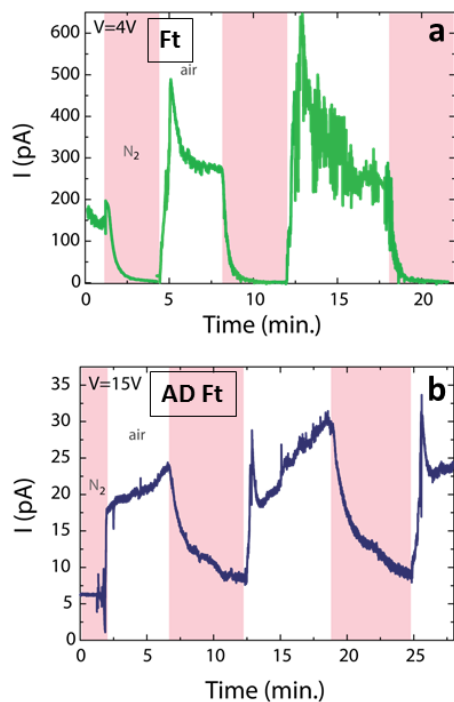


Figure 6.4: Current as a function of time at a fixed applied voltage for a sample with (a) ferritin (ChipA_15 from Figure 2 (c) and (b) ChipB_7 human Alzheimer's ferritin IV is displayed in Figure 2 (d)). Suppression of current is observed when nitrogen is introduced in the chamber for both Ft and AD Ft; the current level re-establishes as soon as the nitrogen has been exchanged with air.

At this stage, we cannot conclude if the difference in electrical properties present in the current studies is related to the impact of the ferritin shell or its core. In case of core-dominant transport the low conductance of the AD Ft samples could be a result of the low number of Fe metal ions in its core. In order to prove that the core (and the number of iron atoms in it) has impact on conductance more systematic study including apoferritin (a ferritin shell without core) and characterization of single proteins should be performed.

6.4. CONCLUSIONS

In conclusion, we have reported on the electrical characterization of Alzheimer's human ferritin. Protein networks, deposited on a chip with two nanoelectrodes, showed an electrical response to the voltage applied across the junction. Noticeably, the current values of Alzheimer's samples at ambient were constantly lower than those of physiological ferritin, used as a reference. This intrinsic conductance difference between pathological and physiological proteins allows to use the electrical characterization and nanoelectrodes as a label-free method for on-a-chip disease recognition. The change in the environment, for instance from ambient to nitrogen gas atmosphere causes a decay in current as the gas was introduced for both types of samples. The current decay appeared to be reversible, when ambient atmosphere was set again the electrical response of both Alzheimer's and normal ferritin went back to their initial values. This environment-dependent current switching can give an insight on fundamentals of protein functioning.

6.5. APPENDIX

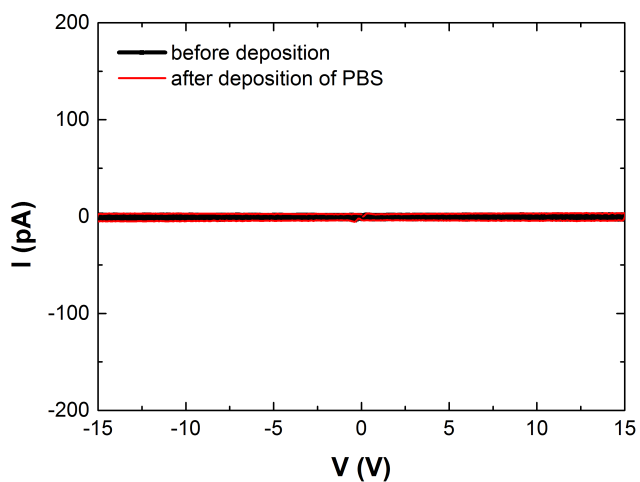


Figure 6.5: Current-voltage (I-V) characteristic of the device before deposition (black line) and after deposition of PBS solution (without ferritin). The current remain below the noise limit of the setup ($<5\text{pA}$), which indicates that PBS after trying out in vacuum is not conductive.

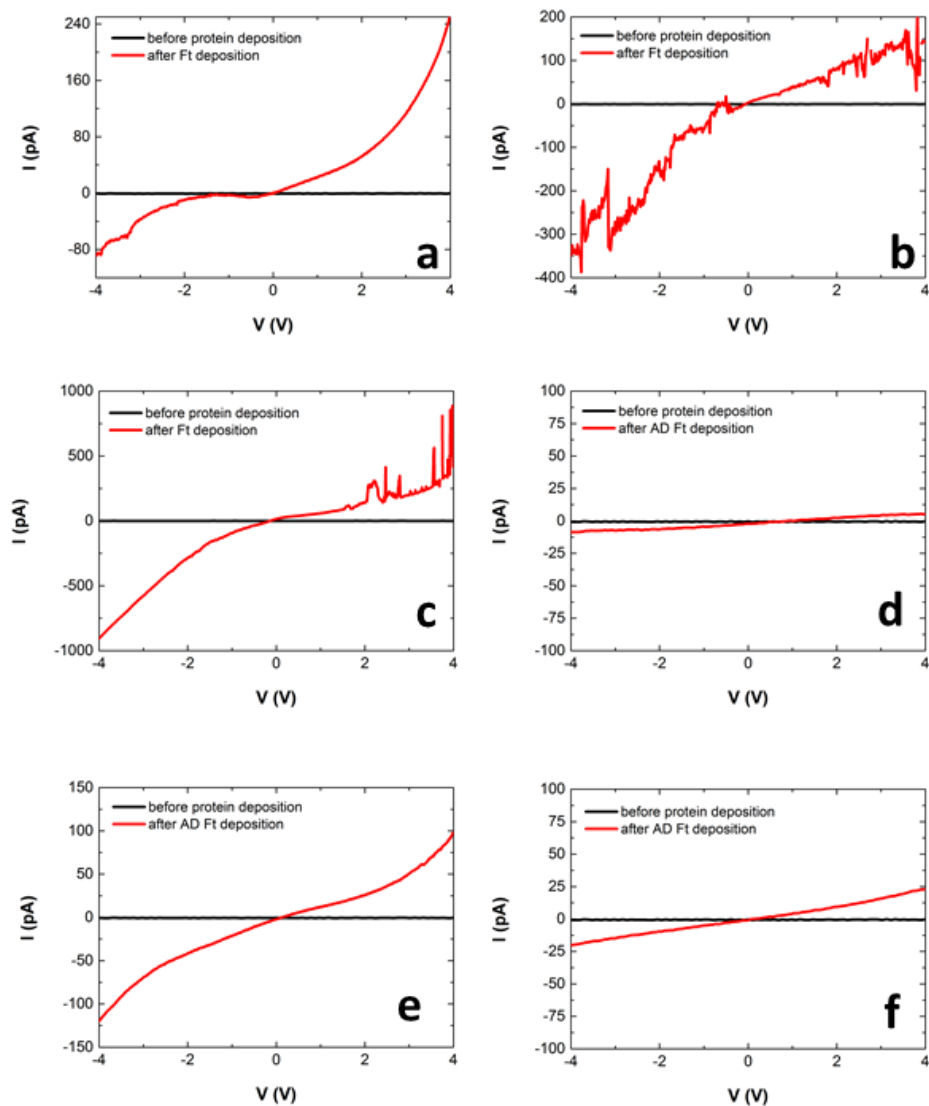


Figure 6.6: Current-voltage (I - V) characteristics of representative devices with Ft ChipA_15(a), ChipA_14 (b), ChipA_12 (c) and AD Ft ChipB_7 (d), ChipB_1 (e), ChipB_3 (f) at $V = 4V$. The current flowing through AD Ft is on average smaller than the one through Ft.

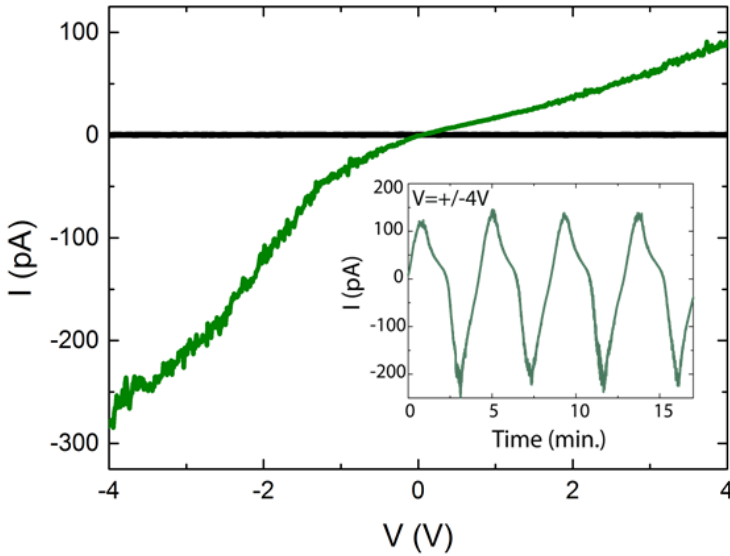


Figure 6.7: I-V measurements for ChipA_13 before deposition (black line), and after Ft deposition (green line) at $V = 4V$. Inset: four consecutive I-Vs taken at $V = 4V$ show that the current values do not change over time.

6

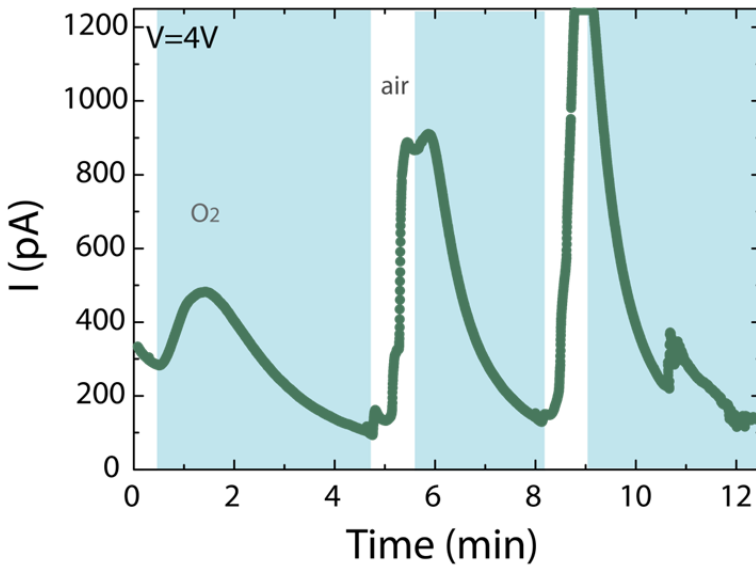


Figure 6.8: Current recorded as a function of time (at $V = 4V$) for the sample ChipA_15. The presence of oxygen (blue regions) suppresses current running through the device.

REFERENCES

- [1] Harrison, P. M. and Arosio, P., *The ferritins: molecular properties, iron storage function and cellular regulation.*, Biochim. Biophys. Acta **1275**, 161–203 (1996).
- [2] Treffry, A., Harrison, P. M., Cleton, M. I., de Bruijn, W. C. and Mann, S., *A note on the composition and properties of ferritin iron cores.*, J. Inorg. Biochem. **31**, 1–6 (1987).
- [3] Honarmand Ebrahimi, K., Bill, E., Hagedoorn, P.-L. and Hagen, W. R., *The catalytic center of ferritin regulates iron storage via Fe(II)-Fe(III) displacement.*, Nat. Chem. Biol. **8**, 941–948 (2012).
- [4] Truffi, M. et al., *Ferritin nanocages: A biological platform for drug delivery, imaging and theranostics in cancer.*, Pharmacol. Res. **107**, 57–65 (2016).
- [5] Meldrum, F. C., Heywood, B. R. and Mann, S., *Magnetoferritin: in vitro synthesis of a novel magnetic protein.*, Science **257**, 522–523 (1992).
- [6] Wong, K. K. W. and Mann, S., *Biomimetic synthesis of cadmium sulfide-ferritin nanocomposites.*, Adv. Mater. **8**, 928–932 (1996).
- [7] Xu, D., Watt, G. D., Harb, J. N. and Davis, R. C., *Electrical Conductivity of Ferritin Proteins by Conductive AFM.*, Nano Lett. **5**, 571–577 (2005).
- [8] Kumar, K. S., Pasula, R. R., Lim, S. and Nijhuis, C. A., *Long-Range Tunneling Processes across Ferritin-Based Junctions.*, Adv. Mater. **28**, 1824–1830 (2016).
- [9] Axford, D. N. and Davis, J. J., *Electron flux through apo-and holoferritin.*, Nanotechnology **18**, 145502 (2007).
- [10] Ayton, S., Faux, N. G. and Bush, A. I., *Ferritin levels in the cerebrospinal fluid predict Alzheimer's disease outcomes and are regulated by APOE.*, Nat. Commun. **6**, 6760 (2015).
- [11] Bossoni, L. et al., *Human brain ferritin studied by muon spin rotation.*, ArXiv170207222 Phys. (2017).
- [12] Gálvez, N. et al., *Comparative Structural and Chemical Studies of Ferritin Cores with Gradual Removal of their Iron Contents.*, J. Am. Chem. Soc. **130**, 8062–8068 (2008).
- [13] Cozzi, A. et al., *Analysis of the biologic functions of H- and L-ferritins in HeLa cells by transfection with siRNAs and cDNAs: evidence for a proliferative role of L-ferritin.*, Blood **103**, 2377–2383 (2004).
- [14] Fleming, J. and Joshi, J. G., *Ferritin: isolation of aluminum-ferritin complex from brain.*, Proc. Natl. Acad. Sci. U. S. A. **84**, 7866–7870 (1987).
- [15] Dedman, D. J. et al., *Iron and aluminium in relation to brain ferritin in normal individuals and Alzheimer's-disease and chronic renal-dialysis patients.*, Biochem. J. **287**, 509–514 (1992).
- [16] Gálvez, N. et al., *Comparative Structural and Chemical Studies of Ferritin Cores with Gradual Removal of their Iron Contents.*, J. Am. Chem. Soc. **130**, 8062–8068 (2008).

7

OUTLOOK

In this chapter we discuss possible follow-up experiments and which applications and opportunities of electrical sensing of the proteins emerge from the studies performed in this thesis. An application-based approach would be the use of nanoelectrodes for biosensing and diagnostics, whereas a fundamental path would consider electrical characterization as a way of systematic studies on the mechanism behind electrical transport in protein and networks made thereof.

7.1. CONDUCTANCE OF IRON-CONTAINING PROTEINS

Figure 1 summarizes typical current values (logarithmic scale) for the five types of iron-containing protein networks highlighted in this thesis. The difference in the current values of these proteins may stem from the fact that the composition or presence of metallic core influences charge transport. Holoferitin, which consists of a protein shell and a metallic core hosting up to 4500 iron atoms, is the most conductive out of five types of proteins studied. Apoferitin on the other hand has no metallic core and is the least conductive one. The samples with Alzheimer's ferritin are in between holo- and apoferitin in terms of conductance. These samples have a metallic core but are not as much loaded with iron atoms as holoferitin; see Figure 2 for a comparison between the three types of ferritin studied. The current values of hemoglobin and hemoglobin S (Figure 1) is of the same order of magnitude: the metal composition of both types of hemoglobin is similar, regardless of the presence of mutated β -subunits in Hb S and this maybe an explanation for the equivalent conductance levels in these proteins.

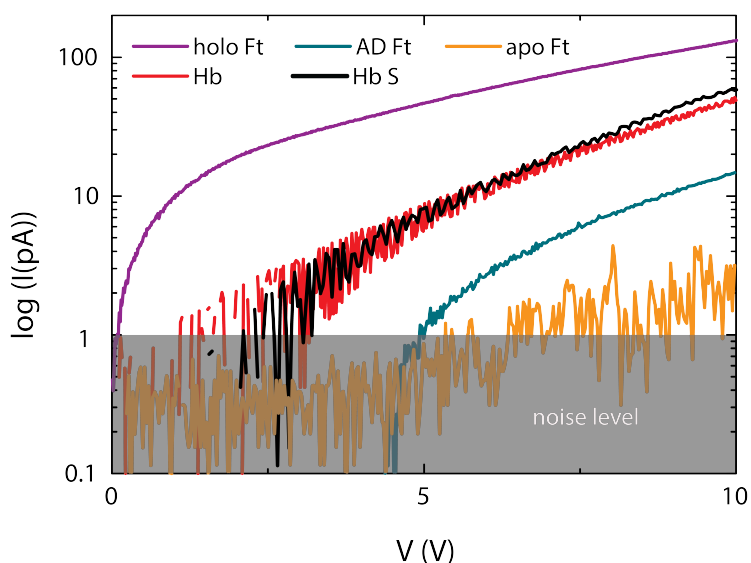


Figure 7.1: (a) Comparison of the representative current-voltage characteristics for iron-containing proteins (holoferitin, apoferitin, AD ferritin, sickle-cell hemoglobin (Hb S) and hemoglobin (Hb)) described in this thesis.

The difference in conductance between normal and abnormal proteins (e.g. Alzheimer's ferritin) can be of use in biosensing or point-of-care devices, so that a disease-diagnostics can be made on a chip by the detection of abnormal proteins of small quantities at an early stage of disease. For higher selectivity proteins could be labelled and nanoelectrodes functionalized such that the coupling of the proteins to electrodes increases, providing a more stable electrical signal and selectivity (only proteins of interest attach to the electrodes out of the essay of proteins deposited onto the chip).

7.2. CONDUCTANCE OF SICKLE-CELL HEMOGLOBIN

In some cases, however, current-voltage measurements are not enough to distinguish normal from abnormal proteins. Then, additional stimuli, such as changes in gas composition, pressure, temperature or irradiation have to be introduced. For instance, in the case of hemoglobin and sickle-cell hemoglobin, Hb S, (see also Figure 3 for details of this protein) the difference in current levels between these proteins appeared to be minimal (Figure 1). In this experiment, the same procedure was followed as for the hemoglobin A0 measurements: the electrodes for contacting Hb S networks were fabricated on Si/SiO₂ wafer using electron-beam lithography and metal evaporation, following the process flow described in Results section of Chapter 6. The Hb S (commercially available from Sigma-Aldrich) was dissolved in DI water (electrical resistivity of 18 M ω -cm), and an aqueous solution containing the Hb S was then deposited onto the chip and placed in vacuum (3×10^{-3} mbar) to let the water to evaporate. The electrical measurements were performed on the devices before and after protein deposition. The recorded current as a function of applied voltage was then compared, and an increase of current after the deposition counted as an indication of protein network being contacted between the two nanoelectrodes.

In Figure 4 a representative example of measured I-V characteristics for hemoglobin S is shown. Before the deposition the current levels were at noise level (below 5pA) and after the deposition an increase of current was observed. In order to check the reproducibility of I-V characteristic stability measurements were performed (Figure 4 inset). A slight decay of current as a function of time was observed. In Chapter 6 we showed that the conductance of hemoglobin networks is environment-dependent. In order to check if this is the case for Hb S networks as well, changes in the environment were applied while measuring the current as a function of time at fixed voltage ($V = 10$ V). As we can see in the Figure 5, current values are hundreds of pA in air, but once vacuum conditions (pressures of 5×10^{-3} mbar or lower) are applied, the current is suppressed and drops below the noise level of our setup (red line in Figure 5). This behaviour was also observed for normal hemoglobin as described in Chapter 5. After vacuum conditions air was pumped back to the chamber while the current was recorded. The current for the abnormal haemoglobin (Hb S) remained below the noise level and didn't recover for the 30 minutes the measurement was performed, while for normal hemoglobin (Chapter 5) the current re-established as soon as air was introduced back into the chamber. Thus, in the cases where proteins of the same family cannot be distinguished directly by means of current levels some, additional stimuli can be applied to reveal the difference in their behaviour. Interestingly, for ferritins the current levels are dependent on the composition of the core, but additional measurements (including magnetic) have to be performed in order to prove this. As we can see from the Figure 1, the conductance of holoferritin (containing up to 4500 iron atoms in its core) is higher than that of apo- or Alzheimer's ferritin. We suggest to perform experiments where the load of the ferritin core is controlled and is varied from a sample with no iron-loaded core to one that has the maximum of amount of iron atoms the core can take up. If the role of the core compositions is important, we expect the current to scale with the number of the iron atoms loaded into ferritin. This would also support the fact that the Alzheimer's (having a mixed iron-II iron-III core) and apoferritin (no iron core) are less conductive

than normal ferritin. For a deeper understanding of the charge transport properties of the proteins and the role of the core and shell therein conductance measurements on a single-protein level could be performed. For this smaller separation lengths between the electrodes should be reached either by using cleanroom techniques or electroburning (see Chapter 3). In this case temperature-dependent electrical measurements could reveal which charge transport scheme is dominant in the protein in combination with other spectroscopic techniques.

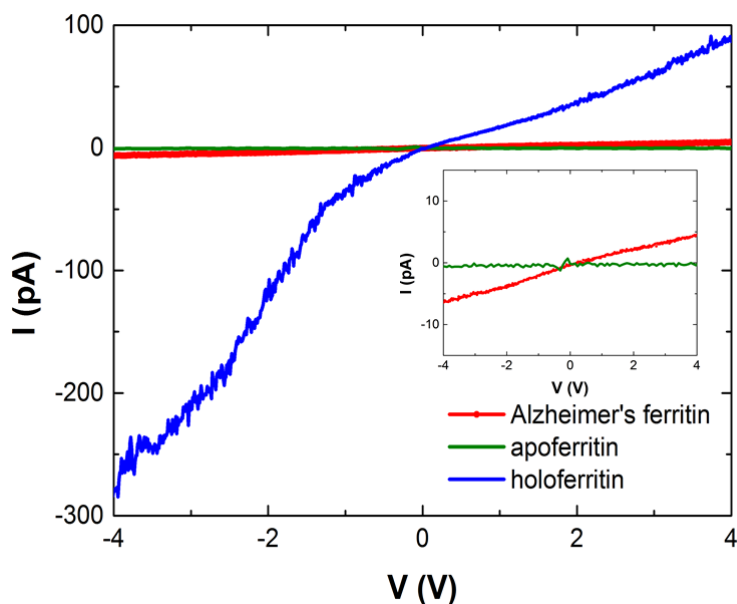


Figure 7.2: Electrical characterization of three types of ferritin thin films: holo-ferritin (blue), apo-ferritin (green) and Alzheimer's ferritin (red). The sample with holo-ferritin exhibits the higher current levels compared to both Alzheimer's and apo-ferritin.

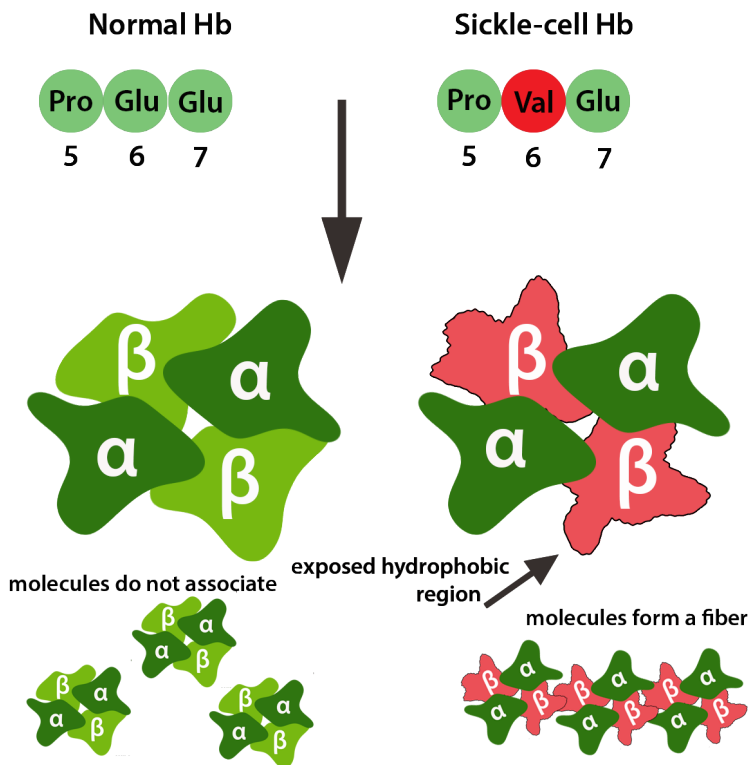


Figure 7.3: Structural differences between hemoglobin (Hb) and sickle-cell hemoglobin (Hb S). A mutation in 6th position of the DNA code causes the creation of mutant subunits in hemoglobin. In these subunits a hydrophobic region is exposed to the outside and this allows the proteins to form fibres, and at the same time decreases their affinity to transport gas molecules.

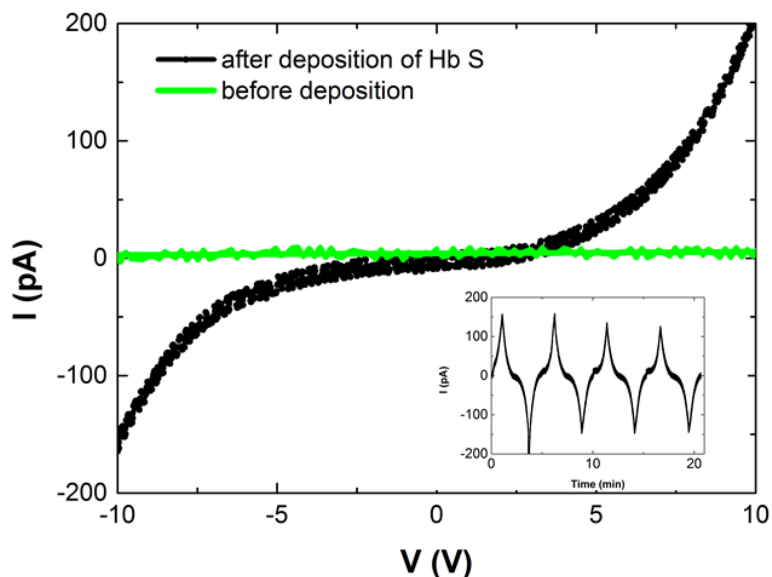


Figure 7.4: Electrical characterization of a sickle-cell hemoglobin (Hb S). The light-green line corresponds to the I-V characteristic before protein deposition, and the black curve represents the I-V after Hb S deposition. Inset: stability plot showing small fluctuations in the current as a function of time.

7

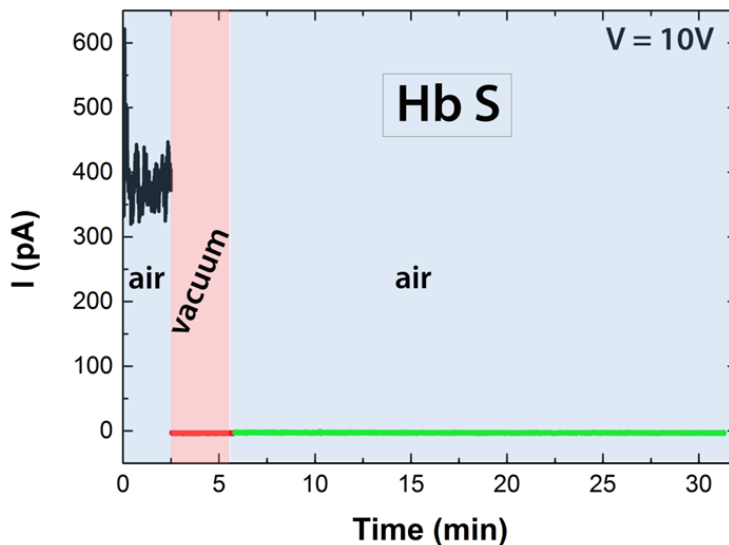


Figure 7.5: Current as a function of time at a fixed voltage ($V = 10V$) for a device with Hb S in air (black line), in vacuum (10-3 mBar; red line), and back to air after vacuum (green line). After going back to air, unlike networks with normal haemoglobin, the sample with Hb S does not recover the current to its initial state (as measured before going to vacuum); it remains for 30 minutes at the noise level of the set-up.

SUMMARY

This thesis describes the research directed towards practical realization of an on-chip biosensing technology and that of understanding charge transport mechanisms in organic and biological nanoobjects. For this, silicon-based chips with metallic nanoelectrodes were fabricated using electron-beam lithography and metal evaporation. The final devices have source-drain separations of tens of nanometres, so that several up to one nanoobject can be trapped in between the electrodes, depending on its size. The electrical characterization is typically performed at room temperature. A current was induced in the sample by applying a voltage across the junction first before the deposition of nanoobject to characterize the bare junction as a reference, and subsequently after deposition. An increase of current after the deposition indicates that nanoobjects participate in the charge carrier flow through the device. For some nanoobjects it was possible to influence the current flow by inducing changes in the environment, for instance by varying the temperature (Chapter 4) or by changing the gas composition (Chapter 5 and Chapter 6). This thesis constitutes the results of two topics: two-dimensional (graphene) electrodes for contacting single nanoobjects (Chapter 3 and Chapter 4), and the electrical characterization of biological iron containing protein networks (Chapter 5 and Chapter 6).

Chapter 2: This chapter gives an introduction to the main technologies used for nanogap formation and contacting nanoobjects. We start by describing a wide range of techniques that are applied for establishing electrical contact to single-nanoobjects and nanometre-thick organic films. We then give more details on the two techniques (electroburning and e-beam lithography) used throughout this work.

Chapter 3: In this chapter, we show that a molecule (diamo-terphenyl) can be coupled to few-layer graphene electrodes. The electrodes were pre-patterned with He-ion beam milling, which allowed to localize the nanogap. In both room-temperature and low-temperature measurements the current increased dramatically after molecule deposition, and the gate sweep showed that the current is dependent on the gate voltage.

Chapter 4: This chapter presents a near-room temperature memory effect in spin-crossover nanoparticles. Single-layer graphene nanogaps formed using e-beam lithography were used for contacting the nanoparticles. Reproducible hysteresis in conductance (of about 40 K) associated with the spin-transition was observed. Noticeably, the low-spin state has a higher conductance than the that of the high-spin state. The detailed analysis of the data showed that the presence of the silica shell may cause the inversion of the activation energies and pre-exponential factor.

Chapter 5: This chapter introduces electrical characterization of hemoglobin protein networks connected to platinum electrodes with 100-nm separation. The reference measurement at ambient conditions shows that the protein networks are conductive. When the environment changes, e.g. changes in gas or pressure, the conductance of the protein network deviates from the reference measurements. In particular, the cur-

rent vanishes in vacuum and shows a decrease when exposed to nitrogen gas instead of air. The Poole-Frenkel emission model has been used to describe the charge transport mechanism with good agreement between the model and the data.

Chapter 6: In this chapter, we compare the conductance of normal human ferritin and Alzheimer's ferritin networks. At ambient conditions the two types of protein, coupled to 100-nm-spaced platinum electrodes, showed different levels of conductance. Moreover, the conductance of the samples with Alzheimer's ferritin is consistently lower than the ones consisting normal protein. When a nitrogen atmosphere was introduced (similar conditions as described in the Chapter 5) the conductance of both proteins went below the detection limit of the setup. It was then recovered again by introducing air to the chamber.

Chapter 7: This chapter discusses potential follow-up experiments and our ongoing work on electrical protein sensing. We show electrical measurements of sickle-cell hemoglobin and compare it with those on normal hemoglobin (from Chapter 5). The current levels of these two types of protein are similar, but the sample with sickle-cell hemoglobin showed no recovery after being in vacuum, unlike the samples with normal hemoglobin in which current levels re-establish after air is pumped back into the chamber. Also, we summarize the typical current values of iron-containing protein networks studied in this thesis. The most conductive one is the holoferritin network comprising of a protein that contains a large number of iron in its core; the least conductive network is that built up from apoferritin. This protein does not have a metallic core.

SAMENVATTING

Dit proefschrift beschrijft onderzoek naar de praktische realisatie van een on-chip biosensing technologie en het begrip van ladingstransport mechanismen in organische en biologische nano-objecten. Hiervoor zijn op silicium gebaseerde microschemelingen met metallische nano-electroden gefabriceerd, gebruikmakend van electron-beam lithografie en het opdampen van metalen. De uiteindelijke devices hebben een source-drain afstand van tientallen nanometers. Afhankelijk van de precieze afstand tussen de elektroden worden een aantal tot een enkel nano-object ingevangen. De elektrische karakterisatie wordt typisch uitgevoerd bij kamertemperatuur. Voorafgaand aan depositie van de nano-objecten wordt een nulmeting uitgevoerd, door een spanning over de elektroden aan te leggen en de opgewekte stroom te meten. Na depositie van de deeltjes wordt dezelfde meting herhaald. Een verhoogde stroom in deze laatste meting wijst op deelname van de nano-objecten aan het ladingstransport door de schakeling. Voor sommige van de onderzochte nanoobjecten bleek het mogelijk de stroom te beïnvloeden door veranderingen in de omgeving aan te brengen, bijvoorbeeld door de temperatuur te variëren (hoofdstuk 4), of door de gassamenstelling te veranderen (Hoofdstuk 5 en Hoofdstuk 6).

Hoofdstuk 2: Dit hoofdstuk introduceert de belangrijkste technologieën die ontwikkeld zijn voor de vorming van openingen op de nanoschaal en voor het contact maken met nano-objecten. We beginnen met een breed overzicht van technieken die gebruikt worden om elektrisch contact te maken met een enkel nano-object en extreem dunne organische lagen. In het bijzonder wordt er een gedetailleerde beschrijving gegeven van de twee technieken die in dit werk gebruikt worden, namelijk electroburning en e-beam lithografie.

Hoofdstuk 3: In dit hoofdstuk laten we zien dat een molecuul (diamo-terphenyl) gekoppeld kan worden aan elektroden bestaande uit enkele lagen grafeen. Om een nanoschaal opening tussen de elektroden te realiseren worden ze voorgevormd, gebruikmakend van een frees gebaseerd op een helium-ionenstraal. Zowel in kamer- als lage-temperatuur metingen neemt de stroom na depositie van de moleculen toe. De stroom blijkt ook afhankelijk te zijn van de spanning op de gate.

Hoofdstuk 4: Dit hoofdstuk presenteert een geheugeneffect in spin-crossover nanodeeltjes dat plaatsvindt dicht bij kamertemperatuur. Om contact te maken met de nanodeeltjes is een nanoschaal opening gemaakt in enkellaags grafeen, gebruikmakend van e-beam lithografie. Bij het variëren van de temperatuur laat de geleiding reproduceerbare hysteresis zien, van ongeveer 40 graden. Deze hysteresis wordt geassocieerd met een verandering van de spintoestand van de nanodeeltjes. Opvallend is dat de lage-spintoestand een hogere geleiding heeft dan de hoge-spintoestand. Een gedetailleerde analyse laat zien dat de aanwezigheid van een silica omhulsel een verklaring kan zijn voor de inversie van de gemeten activatie energiën en de factor voor de exponent, die de geleiding als functie van temperatuur beschrijven.

Hoofdstuk 5: Dit hoofdstuk introduceert de elektrische karakterisatie van hemoglobine eiwitnetwerken in verbinding met platinum elektroden met een 100 nm afstand. De nulmeting bij buitendruk laat zien dat de eiwitnetwerken geleiden. Wanneer de omgeving verandert, bijvoorbeeld door veranderingen in de gassenstelling of druk, laat de geleiding van de netwerken een afwijking van de nulmeting zien. In het bijzonder valt de stroom weg in vacuüm en vermindert die in een stikstofomgeving ten opzichte van een luchtomgeving. Het Poole-Frenkel emissie model is gebruikt om het ladingstransport te beschrijven en laat een goede overeenkomst zien tussen het model en de data.

Hoofdstuk 6: In dit hoofdstuk vergelijken we de geleiding door gezond menselijk ferritine met ferritine netwerken verkregen uit Alzheimerpatiënten. In de buitenlucht hebben de twee type eiwitten, gekoppeld aan platinum elektroden met een afstand van 100 nm, verschillende geleiding. De geleiding door samples met ferritin uit Alzheimerpatiënten is stelselmatig lager dan de geleiding door samples die gezond ferritine bevatten. In een stikstofatmosfeer (vergelijkbare condities als in Hoofdstuk 5) viel de geleiding van beide eiwitten onder het ruisniveau van de opstelling. Door opnieuw lucht in te laten konden de eerdere geleidingsniveaus worden hersteld.

Hoofdstuk 7: Dit hoofdstuk behandelt mogelijke verdere experimenten en ons doorlopende onderzoek aan detectie met elektrische metingen door eiwitten. We presenteren elektrische metingen aan sikkcel hemoglobine en vergelijken deze metingen met de eerdere metingen (Hoofdstuk 5) aan gezond hemoglobine. De hoogte van de stroom in deze netwerken is vergelijkbaar. Echter, in de sikkcel samples herstelden de oude stroomwaarden, na blootstelling aan vacuüm, niet in lucht, in tegenstelling tot de samples met gezond hemoglobine. Daarnaast recapituleren we de typische stroomwaarden van de verschillende ijzer bevattende eiwitnetwerken die bestudeerd zijn in dit proefschrift. De hoogste geleiding is gevonden in het holoferritinnetwerk. Dit eiwit bevat in de kern een grote hoeveelheid ijzeratomen. Het minst geleidende netwerk was opgebouwd uit apoferritine. Dit eiwit bevat geen metallische kern.

ACKNOWLEDGEMENTS

To the people who made an impact in my scientific life...

First of all, and absolutely not surprising, I would like to thank my advisor Herre. I've learnt a lot from you and still keep learning. I was extremely lucky to have a supervisor whose deep knowledge in fundamental physics is combined with application-oriented ideas. During my first intake interview you asked me if I like fundamental physics or applied physics the most. I hesitated with an answer, but now after almost four years I can say that I liked what I was working on, no matter which category it belongs to. Thank you for giving an opportunity to work in your group and for supporting bio-related ideas of mine, which were then converted into successful projects.

Also, I highly appreciate the time that the committee members spent reading my thesis. Prof. Zandbergen, Prof. Dogterom, Prof. Vandersypen, Prof. Steeneken and Prof. Peters thank you for being in the committee.

I would like to thank our secretaries Maria, Dorine and Heleen for their assistance in administrative matters. Maria, thank you for listening to my poor Dutch when I was attempting to practice it, and for your help during my first ("mutation") year in TUD. My cleanroom work won't be as successful without advices and trainings from our Kavli Nanolab staff: Hozanna, Paul, Frank, Roel, Charles, Marco, Ewan, Anja, Arnold, Marc and Eugene.

I would like to acknowledge Enrique Burzuri who was a postdoc in Herre's group when I started. Thank you for sharing your knowledge on charge transport, for your feedback on my data, for reading my first-ever draft of the paper (I can imagine how difficult it was to read it at the beginning, but as you said "someone has to do it anyway"). Also, I'd like to thank Joshua and Max for "babysitting" me in the lab during the first months of measurements. Thank you for your patience and teaching me how to use lab equipment. I'd like to thank Julien, another postdoc in Herre's lab. We worked together on spin-crossover nanoparticles, and I very much appreciated his enthusiasm, expertise in the field and willingness to help. Thank you for bringing me to "nanoparticle world", for taking shifts in the measurements and critical thinking when analysing data.

I also thank my paranymphs and best friends here in the Netherlands: Olga Shevchuk and Alexandra Fursina for providing support and friendship that I needed. Girls, you are an example of successful female scientists who found a balance between work and personal life. "I don't know how she does it" – keeps running in my mind when I hear how busy your days are, and you're catching up with every and each thing in your to-do-list. Olya, I wish you and your young family all the best, and I hope we'll have an opportunity to meet from time to time. Ale, I still remember when Enrique told me that a new postdoc is coming to our group and that new postdoc is you. It has been three/four years since we've met near Aula for the first time. I really enjoyed our lunch conversations

and outings with your daughter Vikki. I wish you best of luck with your future career and life.

It was very interesting to see how the group was expanding and shrinking over the years. To the members of van der Zant Lab: Sabina, I hope your graphene project will be a great success. Ignacio, Davide was a great experience to share the lab with you, especially when the classical music was louder than the noise from the pumps. Rocco, thanks for making the bridges with Leiden and for ferritin project. Joeri and Vera, I enjoyed our conversations during the lunchtime and good luck with your interesting and challenging projects. I'd like to mention some of my colleagues from other groups as well. Ranko, I hope everything goes well with your graduation, patience in learning Dutch and passing the exams, you can do it! Yildiz, was a great pleasure to have you in the neighbouring office and chat during the breaks. Hope to see you graduating in three years from now. Floris and Giordano, thanks for sharing office with me and struggling with heating and sunshine "disasters".

I would like to thank my Russian-speaking friends Maria R., Tatiana K., Masha N., Elena R., Gleb and Katya. It was a pleasure to meet you here in TUD, to share with you ups and downs of an expat life. Now, as we all graduated and found ourselves in different post-PhD jobs wish you all the best and hope to see you around.

My time at TUD was also enriched with lots of fencing trainings and competitions. I would like to thank Deft Fencing Club for the times we were "dying" at the warming-ups and for the great feeling of winning the national medals.

I would like to thank my family: Ihor, Tetyana, Kathrine and Mariia for all their love and encouragement. My dear sister Mariia, I'm sure you find yourself in biology-related field, and maybe one day we could even publish a paper together.

CURRICULUM VITÆ

Anastasia HOLOVCHENKO

08-11-1990 Born in Sumy, the Ukraine.

EDUCATION

2003-2007 High school
School No.27, Sumy, Ukraine

2007-2011 BSc. in Micro- Nanoelectronics
Sumy State University, the Ukraine
Thesis: Nanooptics and Nanophotonics
Supervisor: Dr. V. N. Borysiuk

2011-2012 MSc. Physical and Biomedical Electronics (*cum laude*)
Sumy State University, the Ukraine
Thesis: Towards optimized integrated optomechanical
transducer for ultra-sensitive force measurements
Supervisor: Prof. dr. T. J. Kippenberg, École Polytechnique
Fédérale de Lausanne, Switzerland

2012-2017 PhD
Delft University of Technology, Delft, the Netherlands
Thesis: Electrical characterization of nanoparticle and pro-
tein networks
Promotor: Prof. dr. ir. H. S. J. van der Zant

LIST OF PUBLICATIONS

5. A. I. Holovchenko, M. Koole, E. Burzuri and H. S. J. van der Zant, *Fabrication of a few-layer graphene electrodes for molecular electronics devices*, Proc. NAP **3**, 02NNPT05 (2014).
4. J. O. Island, A. Holovchenko, M. Koole, P. F. A. Alkemade, M. Menelaou, N. Aliaga-Alcalde, E. Burzuri, H. S. J. van der Zant, *Fabrication of hybrid molecular devices using multi-layer graphene break junctions*, J. Phys.: Condens. Matter **26**, 47 (2014).
3. Anastasia Holovchenko, Julien Dugay, Mónica Giménez-Marqués, Ramón Torres-Cavanillas, Eugenio Coronado, Herre S. J. van der Zant, *Near room-temperature memory devices based on hybrid spin-crossover@SiO₂ nanoparticles coupled to single-layer graphene nano-electrodes*, Adv. Mater. **28**, 7228–7233 (2015).
2. Anastasia Holovchenko and Herre S. J. van der Zant, *Environment-dependent conductance measurements on solid-state hemoglobin networks*, submitted (2017).
1. A. Holovchenko, R. Gaudenzi, L. Bossoni, T. H. Oosterkamp and H. S. J. van der Zant, *Conductance measurements on Alzheimer's human brain ferritin*, In preparation for submission (2017).